

Numerical modelling of the micromechanics of sandstone compaction: Developing a Finite Element Model to assess stress-distributions in flat grain-to-grain contacts versus Hertzian point contacts

Arjan de Raad

July 2017

Supervisors

Dr. Cedric Thieulot

Prof. Dr. Christopher Spiers

Dr. Suzanne Hangx



Universiteit Utrecht

Abstract

Reservoir sandstones are highly porous and contain varied amounts of pressurized hydrocarbons and water. The depletion of these reservoirs, i.e. reducing the fluid pressure, increases the effective stresses at the microscale which results in compressive and tensile stresses near grain-to-grain contacts. The response of the individual grains is initially elastic but, if grain-scale stresses become too large, may eventually lead to failure and the grains will show inelastic behaviour causing irrecoverable deformation. This grain-scale deformation translates to compaction of the sandstone reservoir. Thus, these microscale compaction mechanisms initiate deformation at a reservoir scale leading to surface subsidence and microseismicity. The ability to predict the occurrence and the extent of inelastic deformation in such reservoirs is therefore essential to predict future reservoir behaviour. However, the grain-scale behaviour of sand is still poorly understood, especially in terms of stress-distribution across grain-contacts and within grain bodies, which drives grain-scale deformation. Since grain-scale stresses cannot be measured in laboratory experiments, it is needed to model them using numerical codes like Finite Elements. Within this research such a first Finite Element Model is developed for a configuration of simple spherical grains in contact. As a benchmark for the model, a comprehensive description of the Hertzian contact problem is represented addressing all corresponding facets of grain contact modelling at a microscale. The finite element model ELEFANT is tested for elastic behaviour within a single grain using analytical solutions based on the original solution for stresses by Hertz in 1896. The benchmarking of the Finite Element Model ELEFANT produced some satisfactory results as the computed stress- and displacement values by ELEFANT were in good agreement with the analytical solutions.

Contents

| | | |
|----------|--|-----------|
| 1 | Introduction | 5 |
| 1.1 | The Hertzian Contact Theory | 6 |
| 1.2 | Analytical & Theoretical solutions | 6 |
| 1.3 | Grain contact & Packing experiments | 7 |
| 1.4 | Finite Element Modelling | 8 |
| 1.5 | Aims and Objectives | 9 |
| 2 | Methodology | 10 |
| 2.1 | Linearized Theory of Elasticity | 10 |
| 2.1.1 | Stress, Strain & Displacement | 10 |
| 2.1.2 | Hooke's law for linear elastic materials | 12 |
| 2.2 | "ELEFANT" | 14 |
| 2.2.1 | Grid types & Mesh refinement | 15 |
| 3 | Benchmarking FEM "Elefant" for Stress & Strain distributions in elastic media | 16 |
| 3.1 | Simple Shear (2D) | 16 |
| 3.2 | Pure Shear (2D) | 18 |
| 3.3 | J. Becker & M. Bevis, Love's problem (3D) | 19 |
| 3.3.1 | Displacement field | 19 |
| 3.3.2 | Error Analysis | 22 |
| 3.4 | Point load on a Disc (2D) | 24 |
| 4 | Outlook & Discussion | 31 |
| 4.1 | Basic packing model | 31 |
| 4.2 | Mesh refinement | 32 |
| 4.3 | Discussion | 32 |
| 5 | Conclusions | 35 |
| | Appendices | 38 |

List of Figures

| | | |
|----|--|----|
| 1 | Element type Q_1P_0 and P_1P_0 | 15 |
| 2 | Displacement (magnitude) | 16 |
| 3 | Pressure | 17 |
| 4 | Stress in x-direction | 17 |
| 5 | Stress in z-direction | 17 |
| 6 | Displacement in x-direction & z-direction | 18 |
| 7 | Displacement magnitude | 18 |
| 8 | Rectangular lake at the surface of a semi-infinite half-space | 19 |
| 9 | Cross-sections with profile 1 along the x-axis and profile 2 along the y-axis | 20 |
| 10 | Cross-section profile 1 | 21 |
| 11 | Cross-section profile 2 | 21 |
| 12 | Computed displacements and analytical solution (magnitude & X) | 21 |
| 13 | Computed displacements and analytical solution (Y & Z) | 22 |
| 14 | Pressure & strain under applied load | 22 |
| 15 | Error plots of displacement in the direction u, v and w | 22 |
| 16 | L^2 -Norm error plots of the displacements | 23 |
| 17 | Schematic representation of the disc under load | 24 |
| 18 | Cross-sections of pressures through the sphere's center and parallel to both the x- & z-axis | 26 |
| 19 | Cross-sections of σ_{xx} through the sphere's center and parallel to both the x- & z-axis | 26 |
| 20 | Cross-sections of σ_{zz} through the sphere's center and parallel to both the x- & z-axis | 26 |
| 21 | Cross-sections of σ_{xz} through the sphere's center and parallel to both the x- & z-axis | 27 |
| 22 | Cross-sections of the displacements | 27 |
| 23 | Pressure | 28 |
| 24 | Stress tensor (full) σ_{xx} | 28 |
| 25 | Stress tensor (full) σ_{zz} | 28 |
| 26 | Stress tensor (full) σ_{xz} | 29 |
| 27 | Displacements computed by ELEFANT | 29 |
| 28 | Shear stress | 30 |
| 29 | Theoretical and photo-elastic contours of shear stresses (Sadd, 2009) | 30 |
| 30 | Packing configurations with point loading at the contacts | 31 |
| 31 | Photo-elastic fringe patterns for a point loading and a uniform strip load (Johnson, 1987) | 32 |
| 32 | Optres.f90 by Delaunay Triangulation using Triangle | 33 |
| 33 | Delaunay triangulation of sphere boundaries | 33 |
| 34 | Flowchart of program optres.f90 | 42 |
| 35 | Geometry calculations for program optres.f90 | 43 |

1 Introduction

Extraction of hydrocarbons, such as oil and gas, groundwater and geothermal energy from the subsurface can lead to production-related phenomenon after prolonged periods of fluid depletion. Many of such resources can be found in sandstone reservoirs, both onshore and offshore. One of the oldest known cases is the onshore Wilmington Oil Field in California, USA, where 27 years of production resulted in 9m of subsidence. The series of earthquakes in Coalinga, USA, between 1983 and 1987 has also been connected to hydrocarbon production (Suckale, 2009). Besides these two large-scale phenomenon in California, induced seismicity is mostly common in two sedimentary basins elsewhere: 1) the Permian basins in Texas and 2) the Rotliegendes formation (Groningen gas field) in the Netherlands (Suckale, 2009). The Groningen gas field has been subject to an increasing number and intensity of seismic events in the past 10 years due to the depletion of the gas reservoir. Surface subsidence is believed to be caused by compaction of the reservoir at depth. Besides poro-elastic deformation of the reservoir driven by the increase in vertical effective stress caused by depletion, irrecoverable compaction by brittle mechanisms, such as grain cracking or crushing, is expected to occur when the effective stress exceeds a critical value, which generally decreases with increasing aggregate porosity and average grain size (Zhang et al., 1990). As a result, part of the subsidence measured at the surface is likely permanent. In case the reservoir contains faults, differential compaction of the reservoir, caused by lateral variations in the reservoir, can result in differential compaction across faults leading to stress changes which may trigger microseismicity. To predict reservoir compaction and the associated driving forces for induced seismicity, mechanism-based models of sandstone compaction are needed. Micromechanical processes operating at the grainscale determine to a great extent the deformation at the macroscale and can be used to determine reservoir compaction. To predict the macroscale behavior, the stress-strain and strain rate relationships at the grain contact-scale must be understood to model permanent deformation by grain failure and pore collapse (Wong and Baud, 1999). Though these relationships cannot be determined experimentally, existing numerical modelling techniques can be used to study grainscale deformation behaviour.

Previous studies on grain failure mostly include stress and strain distributions at grain contacts incorporating the Hertzian contact theory applied for frictionless, cohesionless, elastic spheres (Zhang et al., 1990) (Brzesowsky, 1995). In short, the theory predicts the generation of a tensile stress at the periphery of the grain contact area leading to grain failure. Hertzian contact theory and linear elastic fracture mechanics (LEFM) (Lawn, 1993) based models have been used to derive analytical models to simulate the deformation behavior of single grain and sand aggregate experiments (Zhang et al., 1990)(Brzesowsky, 1995) to determine the critical load, or applied stress, at failure and the relationship to surface flaws near or outside of the stressed contact area. Such models, incorporating distributed flaw sizes or distributed surface roughness (i.e. asperity size), show physically reasonable results when comparing to experimentally obtained stress and strain behavior (Brzesosky et al., 2011)(Brzesowsky et al., 2014). However, sandstones do not contain cohesionless, point contacts between grains, but rather cemented or truncated/indented grain contacts. For modelling these more complicated grain contacts, finite element modelling of stress distributions at and around cemented grain-to-grain contacts has also been performed (Wong and Baud, 1999). Numerical simulations for cemented grain contacts show smaller magnitude of tensile contacts stresses than uncemented systems, at the same applied stress, making grain failure more difficult. These studies show that different approaches to the micromechanics of compaction in a sandstone result in different stress-strain distributions and locations/modes of grain failure. However, the stress distributions and implications for failure mode at truncated or indented grain contacts in sandstones, formed by pressure solution over geological time, have not been analysed despite the fact that this is the contact structure that most sandstones actually show. Numerical modelling of the elastic stress distribution at such contacts prior to microcrack growth, is therefore urgently needed to provide insight into the micromechanics of deformation and grain scale failure in sandstone.

1.1 The Hertzian Contact Theory

Hertz obtained a complete analytical solution for the stress distribution at and near the contact of two homogeneous isotropic elastic bodies (Brzesowsky, 1995). The theory describes the torsionless loading over a frictional elliptical planar contact area at the end of the diameter along the z-axis. For a Hertzian contact problem the following important assumptions are made (Williams and Dwyer-Joyce, 2001):

- 1) Surfaces are continuous, smooth, nonconforming and frictionless
- 2) The size of the contact area is small compared to the size of the elastic bodies
- 3) The strains within the elastic bodies are small and are within the scope of linear elasticity
- 4) The bodies behave as an elastic half space in the vicinity of the contact area

This ensures that the area outside the contact area are planar and the stress distributions can be calculated without any influence by the boundary conditions (Brzesowsky, 1995). In Cartesian coordinates, the normal stress solution can be given by:

$$[\sigma_{zz}(x, t)]_{z=0} = -\frac{3F}{2\pi ab} \sqrt{1 - x^2/a^2 - y^2/b^2} = -\sigma_0 \sqrt{1 - x^2/a^2 - y^2/b^2} \quad (1)$$

in which σ_0 represents the normal stress at the centre of the contact and a/b are the semi-axes of the elliptical contact area (Hertz, 1896). At the edges of the contact, the stress distribution falls to 0 which is in agreement with Boussinesq's principle for stresses on the surface and outside the origin (Boussinesq, 1885) (Johnson, 1987). If the bodies both possess spherical surfaces the "Hertz-Huber analysis" can be applied, see Brzesowsky (1995). In the case of the contact area (a) becoming very small, the Hertz solution is identical to Boussinesq's solution (see appendix A). The "Hertz-Huber solution" was a unique solution for the contact problem and could be used for any near-field contact problems. The far-field analytical solution was obtained by Sternberg & Rosenthal (1952) and Lurje (1963) for a diametrically loaded sphere. Two equal but oppositely directed point loads F were applied at the end-points of a diameter along the z-axis.

1.2 Analytical & Theoretical solutions

Most experiments and theoretical studies on normal, frictionless contact of linear elastic spheres focus on either the near-field stress distribution (grain surface) using the classical Hertzian theory or on the far-field stress distributions (grain volume). No closed-form analytical solution exists for the complete stress field within a sphere (Titovich and Norris, 2012), especially not for complex grain geometries or different packing systems. Diametric point load studies on circular area's (grain), use the Hertz analysis on concentrated forces (Hertz, 1896) and Boussinesq's stress solution (Boussinesq, 1885) to compute the stress field close to the surface. Hertz's model has one major constraint and assumption, the contact area must be small compared to the radii of curvature. The analytical stress solution can then be derived for the area close to the surface. The far-field stresses are then approximated using numerical modelling or by the superposition of the analytically computed surface stresses (Brzesowsky, 1995). This approach with the superposition of near-field surface stresses was believed to properly predict the far-field stresses because forces acting on a small element would only cause stresses - and strains on the nearest adjacent elements, as Saint-Venant's principle stated (Timoshenko and Goodier, 1970). So far-field stress distributions will not be affected by the loading conditions at the surface. Other far-field stress computations are involved in the complete analytical stress solution by (Liu, 2009) and (Sadd, 2009) for a Hertzian point load between two identical elastic spheres.

1.3 Grain contact & Packing experiments

Hertz's model and many recent studies involve spheres which are under the action of two identical but opposite concentrated loads at the end points of a predetermined diameter. An important constraint in these models is that the contact area between the spheres is very small (point load) compared to the radius of curvature, while sandstones actually show a more flattened contact area between the individual sand grains. As mentioned before, no complete and closed-form analytical solution exist for these contacts. Laboratory experiments on packs of brittle sugar glass discs (Dik, 2016)(Cals et al., 2017) and Plexiglas give great insight in contact-scale deformation mechanisms and show clear grain failure patterns in brittle specimens, but they are not able to visualise the detailed stress distribution within single grain contacts and grain packs. Experimental studies on brittle sugar glass discs show irrecoverable grain failure as the applied stress exceeds the critical failure stress of the samples in both point- as flat grain-to-grain contacts. Dominant failure mechanisms in these discs are tensile intra- and transgranular cracks developing at contact points.

Flattened or indented contact areas have a great influence on the stress distribution. For a given force F a point contact with a smaller contact area will have a higher contact stress. In contrast, a flattened/indented contact will have a larger contact area and a lower contact stress for the same applied force F . Cracks occur at high stress location usually near grain-grain contacts as happened in the experiments executed by (Zhang et al., 1990), (Brzesowsky, 1995) (Brzesosky et al., 2011; Brzesowsky et al., 2014), (Dik, 2016) and (Cals et al., 2017). These microstructural analysis have shown intra-granular and transgranular cracks radiating from the grain's surface and especially from the edges of the contact area. Tensile stresses continue to occur just outside the periphery of the contact and are potential sites for grain failure if the flaw from which the crack propagates is large enough. On the other hand, flattened grain contacts also show cracks initiating from the center of the contact. This is probably due to irregularities along the contact which can act as stress locators similar to a point load. Irregular grains have also been investigated. Brzesowsky et al (2014) experimentally studied the effects of a number of distinct rock parameters on sand aggregates. These parameters, like porosity and grain size, were used to compare the observed trends in sand aggregates to a microphysical model based on the Hertzian contact model and a LEFM (Linear elastic fracture mechanics) model assuming constant flaw size but a distributed radius of curvature. The non-spherical grain pack showed trends which were in best agreement with the LEFM model on stress-strain behaviour (Brzesowsky et al., 2014). Photo-elastic experiments have also been used to explain stress distributions in non-spherical particles under load. Hiramatsu & Oka (1966) investigated three different shapes of photo-elastic epoxy resin to mathematically describe stresses in an irregular test piece subjected to a concentrated diametric load. A theoretical approach to this problem is much more difficult than for a spherical test piece so a 3D photo-elastic experiment was conducted to compare the stress distributions in a spherical test piece with the three irregular test pieces. A mathematical analysis was derived as the tests pieces showed similar stress distributions, within the accuracy of photo-elasticity, for all photo-elastic compression tests. Nonetheless, these experiment are not perfect as the stress distribution in the irregular test piece is not simple and uniform (Hiramatsu and Oka, 1966). Brouwer (2017) also used photo-elasticity in his research on stress distributions. His idea was to use a Finite Element Model to calibrate birefringence patterns to predict stresses in flattened spheres as no analytical solution exists for these contacts. A misfit in the calibration was resolved by the analytical solution of an unflattened sphere by (Liu, 2009) which explained the stress in both the sphere's surface and volume. Stress magnitudes were encountered using this analytical mode for point load stress distributions. A color scheme including magnitudes for the photo-elastic figures was developed using a Michel-Levy chart. This colored birefringence pattern was then extrapolated to the flattened contact so predictions on these stress distributions could be made.

Different packing mechanisms has also been studied using sugar-glass as analogues for sand aggregates (Dik, 2016) & (Cals et al., 2017). Experiments and theoretical approaches incorporating the Hertzian contact theory like (Williams and Dwyer-Joyce, 2001), (Wu and Chau, 2005) and (Titovich and Norris, 2012) but also theoretical studies on far-field stress distributions (Liu, 2009) and (Sadd, 2009) often use a simple cubic packing arrangement in which pressures act at only four contact points. Both studies by Dik (2016) and Cals (2017) focused on different packing mechanisms: simple cubic, hexagonal and a rotated cubic packing (45°). When the applied force is constant, contact stresses are lower in the hexagonal

packing than in the cubic packing due to the additional point contacts increasing the total contact area (Dik, 2016) (Cals et al., 2017). The rotated cubic pack has the same number of point contacts as regular cubic pack but the stress is transferred across the contact area at an angle, instead of diametrically, which may impact the failure behaviour. When comparing stress-strain behaviour with micrographs from sand aggregate experiments flattened, hexagonal or rotated cubic packing show more similarities with these sand aggregates than simple cubic packing (Cals et al., 2017). In addition, hexagonal and rotated cubic packing show grain failure at higher internal stresses than a cubic packing mechanisms so the system itself can be subjected to higher stresses. The actual magnitude of maximum stresses can not be determined. The evolution of cracks and grain failure is therefore difficult to determine. Initial cracks might already be present in grains and could be reactivated when stresses increase. Time independent (instantaneous) compaction mechanisms like elastic deformation, grain breakage coupled with grain rearrangement are usually occurring at the early stages of compaction of sands while time independent mechanisms, such as pressure solution, dominate the final stages (Brzesowsky et al., 2014). Finally, grain size and grain size uniformity also effects the strength of a reservoir as both larger grain size and a higher uniformity leads to higher contact stress en therefore it decreases its strength (Brzesowsky et al., 2014). They all contribute to the micromechanics of sandstone compaction (including porosity and permeability reduction) during the depletion of highly porous reservoir sands and are highly dependent on small but complex variations very near and outside grain contacts.

1.4 Finite Element Modelling

Many elasticity problems with relatively simple geometry can be solved using two-dimensional analytical solutions like in (Sadd, 2009) & (Liu, 2009). Three-dimensional analytical solutions and solutions for more complex geometries are much less abundant and require a numerical evaluation. Most real-world problems involve complex structures for which no analytical solutions exist and therefore a gap exist between what is needed in application and what can be solved analytically (Sadd, 2009). An interesting simulation was done by Wong and Wu (1995). A finite element technique was used to simulate tensile stresses in cemented grain contacts. Cemented contacts enhance the brittle strength of sandstones as intergranular bonds inhibit the relative grain movements. The numerical simulations show a high tensile stress field at the triple junction of the grain, cement and pore space. The magnitude is significantly less than for an uncemented system. The critical value at which grain failure initiates is believed to be an order of magnitude larger than Hertzian's model predicts (Wong and Wu, 1995). Spatial complexity should then be taken into account as even small amount of cement have huge effect on alleviating the tensile concentration, this implies that knowledge on the bulk volume of cement is not favorable as small uncemented areas might exist (unless cementation is very pervasive), and do not experience the protection of cement in intergranular bonding. So information is required on the partial distribution of the cement (Bernabé et al., 1992). A recent discrete element model (DEM) simulated grain failure with resulting grain breakage (Wang et al., 2008). Nonetheless, these models did not incorporate microphysical aspects of grain failure like for instance grain size dependency on stress-strain behaviour while all compaction experiments do describe this phenomenon. Numerical modelling has emerged as one of the methods to provide the necessary accuracy and applicability in stress analysis. It involves the subdivision of a body into a number of elements and subsequently the solution is approximated over these elements. In particular, finite element modelling involves a linear approximation applicable on each single element to develop equations of its elastic behaviour. The general solution is expected to be nonlinear over the entire domain so a piecewise linear approximation is necessary to represent a linear solution over the entire body (Sadd, 2009). Mesh refinement improves the accuracy because a large number of elements represent the solution field. Element size, geometry and approximations scheme's can be varied to suit many problems of different complexity.

Turner et al (2016) numerically modeled a multiple of non-linear relations, like intergranular forces and grain deformation in unconsolidated granular material, by reducing element sizes near contact regions by several order of magnitudes smaller than the grains size. Non-linear relations become nearly linear on such small scales. X-ray tomography was used to accurately capture the 3D morphology and develop a mesh for the Ottawa sand. Additionally a finite element model was developed to numerically model compression in sandstones and to determine the effect of mesh refinement on the stress distributions at grain-to-grain contact. Stresses were determined at the centroid of each tetrahedral element

and were expected to be higher at the contact surfaces similar to Hertzian's model. As in Brzesowsky (2011), this indicates a grain size dependency for grain failure. To inhibit underestimation of stresses near the surface a fine mesh is required (outer 15% of the grain diameter) while a coarser mesh can be used for the volume to increase computer efficiency. The coordination number, the number of contact points with an adjacent grain, effects the amount of stress at these contacts but it is not linearly related to the coordination number. This means that higher density material also inhibits grain failure due to lower stress concentrations at the grain-to-grain contacts and therefore a thinner shell of high resolution meshes is required as the high stress gradient decreased in depth. In addition, computation time decreased using a quadratic tetrahedral element but its high accuracy remained (Turner et al., 2016)

1.5 Aims and Objectives

Many experiments and theoretical analysis's have been performed to gain knowledge on the micromechanics of sand compaction. They all have one or more specific points of interest in what they believe is an important facet in the process of sandstone compaction. Testing the strength of rocks by conventional methods is troublesome since the production of test pieces is very time consuming. These tests have given some satisfactory results (Hiramatsu and Oka, 1966) but none of them is complete, many assumptions had to be made to simplify each analysis. Models often chose idealized spheres to represent a quartz grain or use a predetermined packing density while this is not representative for an actual reservoir sandstone (Turner et al., 2016). The final study and experiments should involve all possible parameters effecting crack evolution and failure including the orientation of each single quartz grain, rotation, sliding and rearrangement. These cracks could be predicted using similar experiments as done by (Brzesowsky, 1995), (Dik, 2016) & (Cals et al., 2017). In addition, failure criterion must be explained in detail to predict fractures and determine critical pressures very precisely. But first, the elastic behaviour within spheres should be properly known.

This study aims to obtain the stress-strain relationship for the deformation of grain-to-grain contacts in sandstones. It will involve high-resolution Finite Element modelling of the micromechanical response of sand grains characterized by a frictional strength plus cohesion to the applied stress conditions. Idealized, spherical isotropic grains (quartz) will behave elastically unless the applied stresses exceed a critical value defined by intergranular friction or by fracture mechanics parameters such as Mode I fracture toughness. The pore fluid will be treated as a low viscosity liquid under hydrostatic pressure. This poro-elastic discretized model will be used

- to investigate stress and strain distributions at and around grain contacts,
- to map stresses along the surface of the grains and within the grain body,
- and thus to identify potential failure sites and mechanisms using fracture mechanics criteria.

Developing these models and assessing their implications for compactive yield, will help determine one of the potential mechanisms resulting in permanent reservoir deformation and provide an improved basis for interpreting experiments. Applied effective stress and porosity will be systematically varied to explore under which conditions the system behaves in a poro-elastic manner versus yielding due to grain slip or failure. These results will be benchmarked against solutions for point contacts, i.e. Hertzian contact theory.

2 Methodology

2.1 Linearized Theory of Elasticity

Linear elasticity, the mathematical description of the linear elastic behavior of material under stress, has been providing simple analytical solutions for many geotechnical problems in engineering as most soils and rocks behave approximately like a linear elastic material (Davis and Selvedurai, 1996). Continuum mechanics form the basis of the nonlinear elasticity equations and are therefore simplified to become linear by the means of two assumptions (Slaughter, 2001):

- infinitesimal strains; only small amounts of strains are accounted for in the solutions
- linear relation between stresses and strains, until plastic deformation starts occurring

These relatively short equations are an advantage when comparing to the more extensive numerical solutions, as they require more known parameters. Linear elastic solutions are then widely used to benchmark computer-based solutions as the exact solution is already known. In addition, these computational models are very dependent on the efficiency of all computations which is therefore a challenge in numerical modelling. Within this chapter the physics and the methodology are explained for the finite element model obtained to visualize tensile stresses in elastic spheres that could initiate crack evolution and failure.

2.1.1 Stress, Strain & Displacement

The theory of elasticity uses many types variables that act on partial points (or nodal points) in a body of specific medium. These variables are either scalar (magnitude), vector quantities (2 or 3 components) like displacement and rotation. Variables like stress and strain are in the form of matrices with often more than 3 components. (Sadd, 2009). A typical 3-dimensional representation of stress will be obtained using a traction vector on a surface subject to an external load.

This section explores the transmission of forces through elastic materials, both boundary and internal, described by traction vectors, stress tensors and equilibrium equations. Maximum stresses are generally the major contributing factor in failure mechanisms so these stresses are important to examine in elasticity studies. Two important groups of forces exist, body forces and surface forces. Body forces refer to forces dependent on the body's mass and acts with for instance gravity-, inertial- and magnetic forces. In continuum mechanics, a body force density can be written as a volume integral over the body (force per unit volume):

$$F = \iiint_V F(x)dV \quad (2)$$

Surface forces act when a body is in contact with another body. Similar like the body force, a surface force is expressed in a surface force density function.

$$F_s = \iint_S T^n(x)dS \quad (3)$$

To quantify the distribution of forces and tractions in a continuum solid, a small area ΔA is subjected to force ΔF with unit vector n .

$$T^n(x, n) = \lim_{\Delta A \rightarrow 0} \frac{\Delta F}{\Delta A} \quad (4)$$

The orientation of the unit normal vector n and the partial location x both affect the traction vector. Integrating over the entire surface area will determine the total surface force. In the case in which ΔA coincides with each three coordinate planes so that each unit normal vector aligns itself along the positive coordinate vector, as is done to discretise certain body's, the traction vectors becomes:

$$\begin{aligned}
T^n(x, n = e_1) &= \sigma_x e_1 + \tau_{xy} e_2 + \tau_{xz} e_3 \\
T^n(x, n = e_2) &= \tau_{yx} e_1 + \sigma_y e_2 + \tau_{yz} e_3 \\
T^n(x, n = e_3) &= \tau_{zx} e_1 + \tau_{zy} e_2 + \sigma_z e_3
\end{aligned} \tag{5}$$

In which e_1, e_2, e_3 are the unit vectors along the three coordinates. From these equations the 9-component stress tensor is obtained.

$$\text{stress matrix} = [\boldsymbol{\sigma}] = \begin{pmatrix} \sigma_x & \tau_{xy} & \tau_{xz} \\ \tau_{yx} & \sigma_y & \tau_{yz} \\ \tau_{zx} & \tau_{zy} & \sigma_z \end{pmatrix}$$

With σ_x, σ_y and σ_z being the normal stresses and $\tau_{xy}, \tau_{yx}, \tau_{yz}, \tau_{zy}, \tau_{xz}$ and τ_{zx} being the shear stresses. Notice that positive normal stresses act as tensile stresses. The internal stress field is in moment equilibrium as the tensor is symmetrical.

The displacements in these bodies as a result of an applied load can be presented in elastic field equations. The kinematics of material deformation is basically the response of a material. These deformations can be quantified by the displacements of single material points within the material, a displacement field and a strain tensor which is obtained as they are closely related. The displacement vectors of a point within a solid is obtained using a Taylor series expansion, high orders are left out since the relative position vector r is small:

$$\begin{aligned}
u &= u^0 + \frac{\delta u}{\delta x} r_x + \frac{\delta u}{\delta y} r_y + \frac{\delta u}{\delta z} r_z \\
v &= v^0 + \frac{\delta v}{\delta x} r_x + \frac{\delta v}{\delta y} r_y + \frac{\delta v}{\delta z} r_z \\
w &= w^0 + \frac{\delta w}{\delta x} r_x + \frac{\delta w}{\delta y} r_y + \frac{\delta w}{\delta z} r_z
\end{aligned} \tag{6}$$

where u, v, w are the components (cartesian) of the displacement vector (Sadd, 2009). The displacement gradient tensor is then written as:

$$\begin{aligned}
u_{i,j} &= \begin{pmatrix} \frac{\delta u}{\delta x} & \frac{\delta u}{\delta y} & \frac{\delta u}{\delta z} \\ \frac{\delta v}{\delta x} & \frac{\delta v}{\delta y} & \frac{\delta v}{\delta z} \\ \frac{\delta w}{\delta x} & \frac{\delta w}{\delta y} & \frac{\delta w}{\delta z} \end{pmatrix} \\
u_{i,j} &= e_{ij} + \omega_{ij}
\end{aligned} \tag{7}$$

in which e_{ij} is the strain tensor (symmetric) and ω_{ij} is the rotation tensor (antisymmetric). These relation indicate that for small deformations the change in the relative position vector can be expressed by the the sum of strains and rotations (Sadd, 2009). The general result with $r_i = d_{x_i}$ becomes:

$$u_i = u_i^0 + e_{ij} dx_j + \omega_{ij} dx_j \tag{8}$$

Small deformations can be expressed using more specific strain-displacement relations in which elasticity variables and other field quantities are defined in each infinitesimal element and eventually a single point in a material continuum. Compatibility equations ensure that the strain field consist of only single-valued continuous displacements (Sadd, 2009). The normal- and shearing strain components are these six relations:

$$\begin{aligned}
e_x &= \frac{\delta u}{\delta x}, \quad e_y = \frac{\delta v}{\delta y}, \quad e_z = \frac{\delta w}{\delta z} \\
e_{xy} &= \frac{1}{2} \left(\frac{\delta u}{\delta y} + \frac{\delta v}{\delta x} \right), \quad e_{yz} = \frac{1}{2} \left(\frac{\delta v}{\delta z} + \frac{\delta w}{\delta y} \right), \quad e_{zx} = \frac{1}{2} \left(\frac{\delta w}{\delta x} + \frac{\delta u}{\delta z} \right)
\end{aligned} \tag{9}$$

The strain matrix can also be written in compact form and in direct vector/matrix notation respectively:

$$e_{ij} = \frac{1}{2}(u_{i,j} + u_{j,i}), \quad e = \frac{1}{2}[\nabla \mathbf{u} + (\nabla \mathbf{u})^t] \tag{10}$$

Additional field equations are needed because not all unknowns can be computed with these obtained stress and strain relations. For small deformations the material response of a linear elastic material could provide additional equations to solve for all unknowns. These constitutive relations were obtained using a simple material model "elastic solid" which uses the principles of continuum mechanics and regains its original shape when loading's are removed and strains are linear. These simplified loading tests have shown good agreement with experimental data under small deformations (Sadd, 2009). The next section will explain the three-dimensional constitutive relation for elastic materials.

2.1.2 Hooke's law for linear elastic materials

Hooke's law for linear elastic materials assumes that each stress component is linear related to each strain component:

$$\begin{aligned}
\sigma_x &= C_{11}e_x + C_{12}e_y + C_{13}e_z + 2C_{14}e_{xy} + 2C_{15}e_{yz} + 2C_{16}e_{zx} \\
\sigma_y &= C_{21}e_x + C_{22}e_y + C_{23}e_z + 2C_{24}e_{xy} + 2C_{25}e_{yz} + 2C_{26}e_{zx} \\
\sigma_z &= C_{31}e_x + C_{32}e_y + C_{33}e_z + 2C_{34}e_{xy} + 2C_{35}e_{yz} + 2C_{36}e_{zx} \\
\tau_{xy} &= C_{41}e_x + C_{42}e_y + C_{43}e_z + 2C_{44}e_{xy} + 2C_{45}e_{yz} + 2C_{46}e_{zx} \\
\tau_{yz} &= C_{51}e_x + C_{52}e_y + C_{53}e_z + 2C_{54}e_{xy} + 2C_{55}e_{yz} + 2C_{56}e_{zx} \\
\tau_{zx} &= C_{61}e_x + C_{62}e_y + C_{63}e_z + 2C_{64}e_{xy} + 2C_{65}e_{yz} + 2C_{66}e_{zx}
\end{aligned} \tag{11}$$

In which the coefficient C_{ij} are material parameters. The factor 2 arises from the strain symmetry in the tensor. In standard tensor notation this relation becomes:

$$\sigma_{ij} = C_{ijkl}e_{kl} \tag{12}$$

in which C_{ijkl} is a fourth-order elasticity tensor with all necessary characterization parameters of an elastic material. In homogeneous materials all these elastic moduli are constant. The isotropic stress-strain relations can then be established as the tensor is similar for all rotations. The generalized Hooke's law for isotropic linear elastic solids is given by:

$$\sigma_{ij} = \lambda e_{kk}\delta_{ij} + 2\mu e_{ij} \tag{13}$$

with λ is lamé's constant and μ is the shear modulus. The shear modulus (GPa) describes the materials response to shear stresses. In these isotropic materials strains can be explained by the modes of strains, volumetric strain from the normal stresses and shear strain from shear stresses. The stress tensor σ_{ij} consists of a sum of the normal isotropic stress tensor and a deviatoric shear stress tensor (τ_{ij}) and are related by:

$$\tau_{ij} = \sigma_{ij} - \frac{1}{3}\sigma_{kk}\delta_{ij} = 2\mu \left(e_{ij} - \frac{1}{3}e_{kk}\delta_{ij} \right) \tag{14}$$

Together with equation (13), (14) and the deviatoric shear strain $\hat{e} = e_{ij} - \frac{1}{3}e_{kk}\delta_{ij}$ a relation is obtained for the deviatoric stress and deviatoric shear strain:

$$\tau_{ij} = 2\mu \hat{e}_{ij} \tag{15}$$

To express the strain in terms of stress the relation $\sigma_{kk} = (3\lambda + 2\mu)e_{kk}$ can be used and solved for the normal strain e_{kk} , notice that the free indices are the same. Substitution of this relation into Hooke's general law provides a solution for the strain:

$$e_{ij} = \frac{1 + \nu}{E}\sigma_{ij} - \frac{\nu}{E}\sigma_{kk}\delta_{ij} \quad (16)$$

With the modulus of elasticity E in GPa (also Young's modulus), describing the materials strain response to uniaxial stress in the direction of the stress. The Poisson's ratio ν describes the response in the direction orthogonal to uniaxial stresses. $E = \mu(3\lambda + 2\mu)/(\lambda + \mu)$ and $\nu = \lambda/[2(\lambda + \mu)]$

Using Hooke's law for strain-displacement relations a displacement solution can be obtained using only displacement boundary conditions. So combining the strain-displacement equations and the constitutive equations to eliminate the strain field will result in a stress field with only scalar terms similar to those of the displacement field:

$$\sigma_{ij} = \mu(u_{i,j} + u_{j,i} + \lambda u_{k,k}\delta_{i,j}) \quad (17)$$

Which can be rewritten in 6 scalar equations:

$$\begin{aligned} \sigma_x &= \lambda\left(\frac{\partial u}{\partial x} + \frac{\partial v}{\partial y} + \frac{\partial w}{\partial z}\right) + 2\mu\frac{\partial u}{\partial x} \\ \sigma_y &= \lambda\left(\frac{\partial u}{\partial x} + \frac{\partial v}{\partial y} + \frac{\partial w}{\partial z}\right) + 2\mu\frac{\partial v}{\partial y} \\ \sigma_z &= \lambda\left(\frac{\partial u}{\partial x} + \frac{\partial v}{\partial y} + \frac{\partial w}{\partial z}\right) + 2\mu\frac{\partial w}{\partial z} \\ \tau_{xy} &= \mu\left(\frac{\partial u}{\partial y} + \frac{\partial v}{\partial x}\right), \tau_{yz} = \mu\left(\frac{\partial v}{\partial z} + \frac{\partial w}{\partial y}\right), \tau_{zx} = \mu\left(\frac{\partial w}{\partial x} + \frac{\partial u}{\partial z}\right) \end{aligned} \quad (18)$$

Using these relations and substituting them into the equilibrium equations, the result becomes Navier-lamé's equation:

$$\begin{aligned} (\lambda + \mu)u_{k,ki} + \mu u_{i,jj} + F_i &= 0 \\ (\lambda + \mu)\nabla(\nabla \cdot \mathbf{u}) + \mu\nabla^2\mathbf{u} + \mathbf{F} &= 0 \end{aligned} \quad (19)$$

For the three directions (x, y & z):

$$\begin{aligned} \mu\nabla^2 u + (\lambda + \mu)\frac{\partial}{\partial x}\left(\frac{\partial u}{\partial x} + \frac{\partial v}{\partial y} + \frac{\partial w}{\partial z}\right) + F_x &= 0 \\ \mu\nabla^2 v + (\lambda + \mu)\frac{\partial}{\partial y}\left(\frac{\partial u}{\partial x} + \frac{\partial v}{\partial y} + \frac{\partial w}{\partial z}\right) + F_y &= 0 \\ \mu\nabla^2 w + (\lambda + \mu)\frac{\partial}{\partial z}\left(\frac{\partial u}{\partial x} + \frac{\partial v}{\partial y} + \frac{\partial w}{\partial z}\right) + F_z &= 0 \end{aligned} \quad (20)$$

2.2 "ELEFANT"

For this project a finite element model is developed to properly quantify stresses-strains and potential failure sites in a simplified grain arrangement. The Fortran code "ELEFANT" (Thieulot, 2014) is used to compute the geodynamics by solving the classical 2D/3D momentum conservation equation (21), also known as Stokes equation, to find pressure- and velocity fields or the displacement field in this case. Inertial forces are negligible compared to viscous forces and therefore this momentum equation is reduced to this form. ELEFANT has previously been used to solve several elastic, viscoplastic and viscoelastic problems incorporating elastic responses of materials.

$$\nabla \cdot \boldsymbol{\sigma} + \mathbf{b} = \mathbf{0} \quad (21)$$

With $\boldsymbol{\sigma}$ being the stress tensor and \mathbf{b} being the body forces in terms of gravity ($\rho\mathbf{g}$). The stresses in an elastic medium are related to the strains by the generalised Hooke's law:

$$\boldsymbol{\sigma} = \lambda(\nabla \cdot \mathbf{u})\mathbf{1} + 2\mu\boldsymbol{\epsilon}$$

In which lamé's parameter λ , shear modulus μ are the elastic parameters and $\nabla \cdot \mathbf{u}$ is the isotropic dilation. The strain tensor - displacement relation subsequently becomes:

$$\boldsymbol{\epsilon} = \frac{1}{2}(\nabla\mathbf{u} + (\nabla\mathbf{u})^T)$$

The incompressibility or bulk modulus K can be obtained using the relation $p = -K\nabla\mathbf{u}$ with

$$p = -[\lambda + \frac{2}{3}\mu](\nabla \cdot \mathbf{u})$$

K therefore becomes $\lambda + \frac{2}{3}\mu$. In case of viscous flow, as mentioned at the beginning of this section, μ represents the dynamic viscosity and u represents the velocity as these equations are analogues to one another. All elastic moduli (K, E, λ, μ and ν) are related for a homogeneous isotropic elastic medium. With any two, all others can be calculated. For instance, the Lamé parameter and shear modulus are also linked to the Poisson ratio and the young modulus by:

$$\lambda = \mu \frac{2\nu}{1-2\nu} = \frac{\nu E}{(1+\nu)(1-2\nu)}$$

with $E = 2\mu(1+\nu)$. The discretisation in the finite element method solves for all nodal displacements d to obtain u within the elements:

$$\mathbf{K} \cdot \mathbf{d} = \mathbf{F} \quad (22)$$

In which \mathbf{K} is the global stiffness matrix, d the global nodal displacement vector and F the global nodal force vector. The global K matrix forms from the integral:

$$k_{ab}^e = \int_{\Omega_a} B_a^T D B_b d\Omega$$

Where Ω represents the element volume or surface (similar in 3D & 2D), a and b are the local node numbers. Matrix B_a is defined as:

$$B_a = \begin{pmatrix} \frac{\partial N_a}{\partial x} & 0 \\ 0 & \frac{\partial N_a}{\partial y} \\ \frac{\partial N_a}{\partial y} & \frac{\partial N_a}{\partial x} \end{pmatrix} \quad (23)$$

In 2D, for isotropic materials, the plane strain approximation \mathbf{D} is given in matrix form by:

$$\mathbf{D} = \begin{pmatrix} \lambda + 2\mu & \lambda & 0 \\ \lambda & \lambda + 2\mu & 0 \\ 0 & 0 & \mu \end{pmatrix} \quad (24)$$

The elimination of the unknown pressure in the stokes equation by this penalty method replaces the original saddle-point problem by an elliptical problem leading to a symmetrical positive FEM matrix (Donea and Huerta, 2003).

2.2.1 Grid types & Mesh refinement

Different grid types serve different modelling purposes in either 2D or 3D. Dimensions of domains are of size $L_x \times L_y \times L_z$ and the corresponding finite element grid consist of $n_{cellx} \times n_{celly} \times n_{cellz}$ elements and $nnx \times nny \times nnz$ nodal points. The position vector $r = (x, y, z)$, the velocity vector $v = (u, v, w)$ together with the 6 boundary conditions at the edges of the domain form the input for the grid set-up. A number of function- and subroutine files are needed to create an output- or visualisation file (.vtu). The *read_experiment.f90* file comprises all adjustable features incorporating domain- and element sizes (mesh refinement), grid type, boundary conditions and the finite element method including solver type. The subroutine *analytical_solution.f90* may be called in the *read_experiment* when such analysis is required. The element types are different for each experiment. For the benchmarking of this analysis two element types have been used: a linear quadrilateral/hexahedron element and a linear triangle/tetrahedron element (figure 1). The Q_1P_0 element is used for simple cartesian box geometries (both 2D and 3D) and contains 4 nodes for velocity with 2 degrees of freedom (DOF).

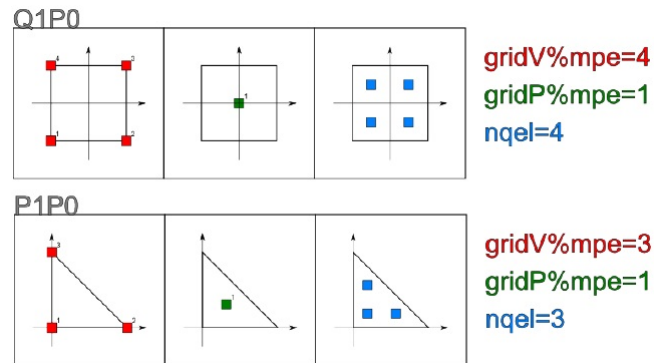


Figure 1: Element type Q_1P_0 and P_1P_0

3 Benchmarking FEM "Elefant" for Stress & Strain distributions in elastic media

The benchmarking of the finite element model ELEFANT for elastic stress- and strain tests will contain four experiments in succession with increasing extent and difficulty. The first two experiments, simple- and pure shear, are executed in 2D comparing the analytical solution for both stress and displacement to the finite element solution. The third experiment, Love's problem (Becker and Bevis, 2004) describes the stress, strain, pressure and displacement in a 3D model as an extensive analytical solution is represented for these quantities. The final tests include a point load at the sphere's surface to represent a simplified configuration of a porous sandstone formation under load. These compression tests will provide insight in the micromechanics of reservoir compaction up to grain failure.

3.1 Simple Shear (2D)

Simple shear deformation explains the constant-volume strain in which a set of line elements with a given reference orientation do not change in length or in orientation when a force is applied. For this experiment the bottom horizontal edge of the square box is fixed and therefore the other sides undergo deformation in terms of orientation, resulting in a rotation of the finite strain axis. The sides of the square are of length 1 ($Lx = 1$ and $Lz = 1$). The displacement solution is then given by:

$$u = \frac{vxbc}{Lz} \times z, \quad (25)$$

$$v = 0, \quad (26)$$

$$w = 0, \quad (27)$$

In which u, v and w are the displacements in each direction (Cartesian reference frame), Lz the total length in the z -direction and z the ascending z -coordinates (0 at the bottom boundary, 1 at the top boundary). $Vxbc$ is the boundary condition for the displacement in x -direction at $Lz = 1$, of magnitude 1. The other boundary conditions are 0 for both u and w . The shear modulus μ is set to 0 and the poisson ratio ν is set to 0.2.

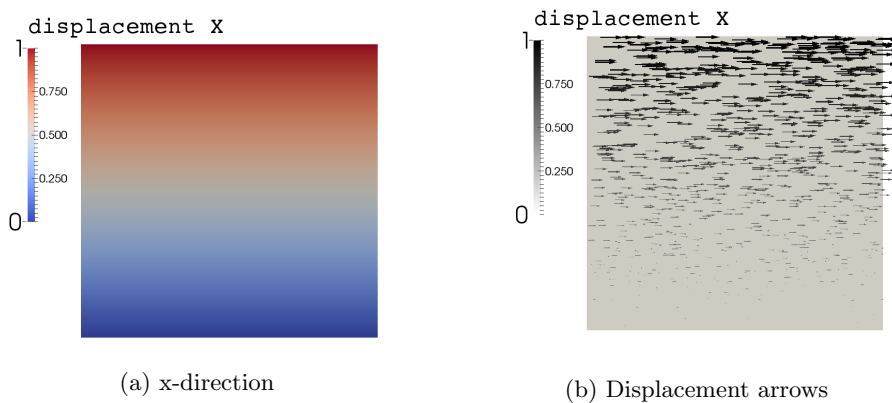
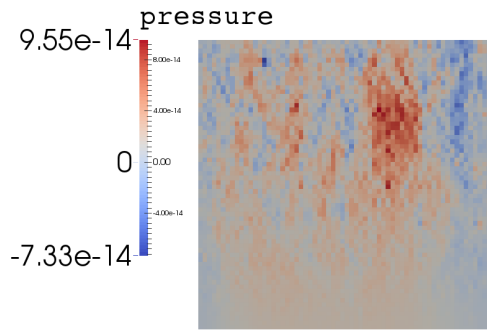
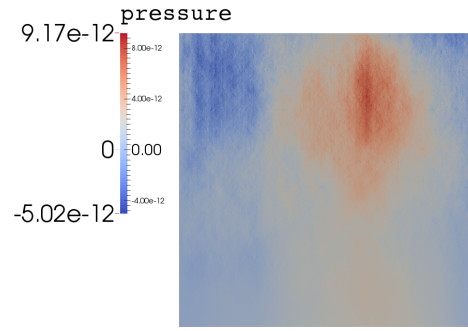


Figure 2: Displacement (magnitude)

The displacements in the x -direction show the expected results, a displacement of magnitude 1 at $z = Lz$ decreasing as z falls to zero (figure 2). The representation of the displacements are identical for both FEM as for the analytical solution. There is no displacement in the z -direction.

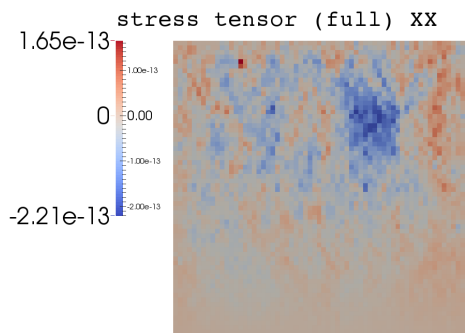


(a) low resolution

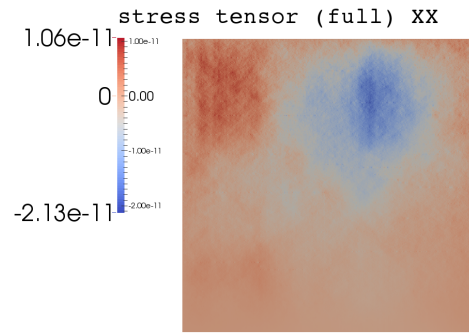


(b) high resolution

Figure 3: Pressure

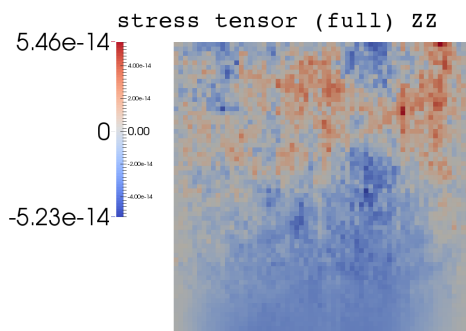


(a) low resolution

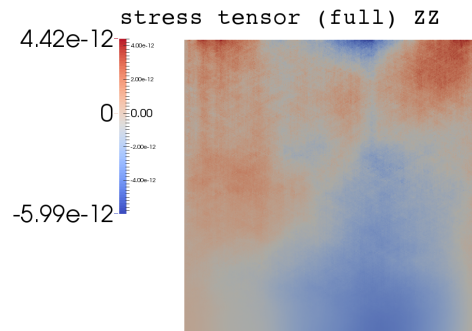


(b) high resolution

Figure 4: Stress in x-direction



(a) low resolution



(b) high resolution

Figure 5: Stress in z-direction

The pressure (figure 3) and stresses in both the x- and z-direction (figure 4 & 5) have been numerically modeled. The pressure is computed for the centres of each element. The smoothing is clearly visible when adjusting the resolution, low resolution means 64 elements in any direction and high resolution means 564 elements in any direction. The high resolution model also shows larger maximum and minimum stresses. Even higher resolution (ncellx=1064 & ncellz=2064) have been tested showing a similar pattern but with no additional smoothing effect. Higher resolution do unfortunately require significantly longer computational time.

3.2 Pure Shear (2D)

Pure shear deformation explains the constant-volume strain in which a body elongates in one direction and shortens in the perpendicular direction. During pure shear, in contrast to simple shear, the axes of the strain ellipsoid do not rotate. The incremental and finite strain ellipsoids are therefore coaxial. This experiment is very similar to the simple shear experiment in terms of dimensions, the difference is the applied horizontal load as there are two in opposite direction. The analytical displacement solution is given by:

$$u = \frac{vxbc}{Lx} * (x - Lx) + x, \quad (28)$$

$$v = 0, \quad (29)$$

$$w = \frac{vzbc}{Lz} * (Lz - z) - z, \quad (30)$$

In which u, v and w are the displacements in each direction (Cartesian reference frame) and Lx & Lz are the total boundary lengths in the x-direction and z-direction respectively. x & z are the ascending x- and z-coordinates. $Vxbc$ is the boundary condition for the maximum displacements in x-direction at $Lx = 1$ and $Lx = -1$, of magnitude 1. $Vzbc$ is the boundary condition for the maximum displacement in the z-direction at $Lz = 1$ and $Lz = -1$, of again magnitude 1.

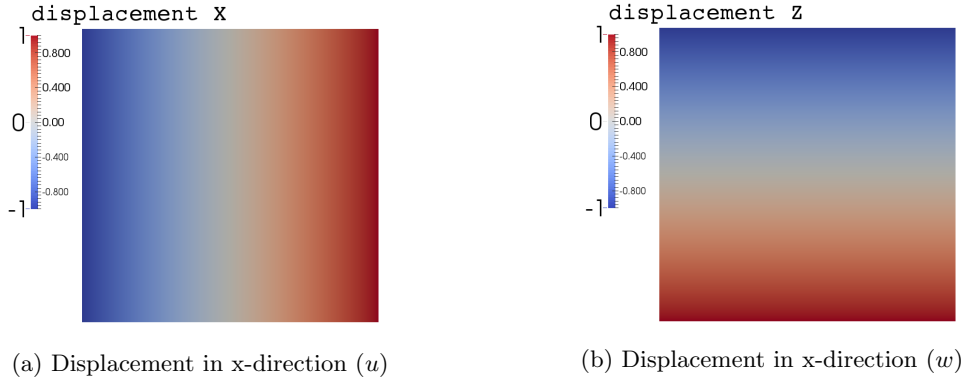


Figure 6: Displacement in x-direction & z-direction

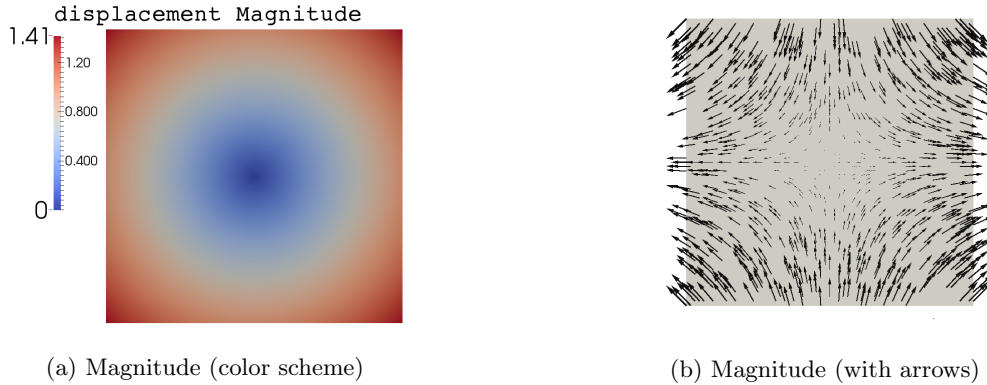


Figure 7: Displacement magnitude

The displacements in the x-direction and z-direction (figure 6) show the expected results, a displacement of magnitude 1 at $x = 0, x = Lx, z = 0$ and $z = Lz$ decreasing towards the center of the box with zero displacement (figure 7). The representation of the displacements are identical for both FEM as for the analytical solution. The computed values for the principle stresses σ_{xx} and σ_{zz} are 4 and -4 respectively, and the shear stress σ_{xz} is 0

3.3 J. Becker & M. Bevis, Love's problem (3D)

For this experiment the article by Becker et al is used. Explicit expressions for displacement in a homogeneous isotropic semi infinite half space (Cartesian) have been obtained. The applied force is a uniform surface pressure over a rectangular area referred to as Love's problem. The problem uses Boussinesq's idea of stresses and displacements being expressed in terms of spatial derivatives of elastic potential functions (Becker and Bevis, 2004). Boussinesq obtained the solution for a point load in 1885 (see appendix B). Different studies within the area of the elasticity theory produced explicit expressions for stresses and displacements under uniform pressures applied by circular loads (Love, 1929). Love (1929) revisited the circular load theory and used Boussinesq's potential method to obtain expressions for the stress but he did not provide expressions for the displacement field. By solving these equations the displacement field for a uniform rectangular load is obtained. Becker et al (2004) produced these expressions for the case of a rectangular load.

3.3.1 Displacement field

Displacements in this experiment are the result of an applied pressure P within a rectangular region (or lake) at the surface ($z=0$) of a semi-infinite elastic half-space with: $-a \leq x \leq a$, $-b \leq y \leq b$ and $z = h$ referring to the depth of the lake (figure 8). The dimensions of the lake are: 2000m ($2 \times a$) by 1000m ($2 \times b$) by 100m(z). The value of z increases with depth (0 at the surface and $z=100$ at the bottom). The entire domain is 10 x 10 x 2.5km and is fixed in order to keep computations manageable. The resolution can be increased by increasing the number of elements in each direction. x, y and z are the coordinates of any point in the solid, $x', y', 0$ is the projectory of that point on the plane boundary with the distance (r) between these points, $r^2 = \Delta x^2 + \Delta y^2 + \Delta z^2$.

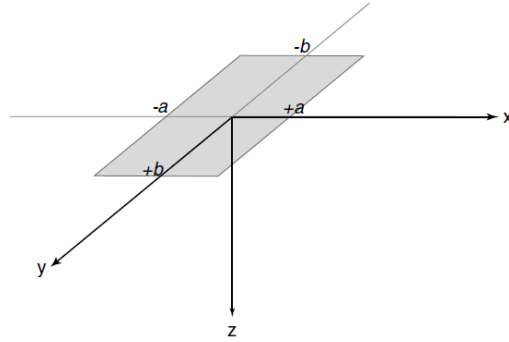


Figure 8: Rectangular lake at the surface of a semi-infinite half-space

The Young's modulus is calculated using: $E = \frac{\mu(3\lambda+2\mu)}{\lambda+\mu} = 0.6 * 10^{11} \text{ Nm}^{-2}$ and the Poisson's ratio $\nu = \frac{\lambda}{2(\lambda+\mu)} = 0.25$. The boundary condition at the surface is given by $P = \rho gh$, with $\rho = 1000 \text{ kg m}^{-3}$, $h = 100 \text{ m}$, and $g = 9.82 \text{ m s}^{-2}$. The boundary conditions at the sides and at the bottom of the domain are prescribed using the analytical solution for displacement.

For the displacement solution (horizontal and vertical) the following relations are needed:

$$\begin{aligned} \psi_{j0} &= \frac{\Delta y}{r_{j0} + \beta_{j0}}, & \psi_{j0}^2 &< 1 \quad (j = 1, 2), & \psi_{0j} &= \frac{\Delta x}{r_{0j} + \beta_{0j}}, & \psi_{0j}^2 &< 1 \quad (j = 1, 2), \\ r_{j0}^2 &= r^2|_{x'=\pm a} = (a \mp x)^2 + \Delta y^2 + z^2, & r_{j0} &> 0, \\ r_{0j}^2 &= r^2|_{y'=\pm b} = (b \mp y)^2 + \Delta x^2 + z^2, & r_{0j} &> 0, \\ \beta_{j0}^2 &= r_{j0}^2 - \Delta y^2 = (a \mp x)^2 + z^2, & \beta_{j0} &> 0, \\ \beta_{0j}^2 &= r_{0j}^2 - \Delta x^2 = (b \mp y)^2 + z^2, & \beta_{0j} &> 0, \end{aligned}$$

The horizontal displacements are:

$$u = -\frac{p}{4\pi} \left[\frac{1}{\lambda + \mu} (J_2 - J_1) + \frac{z}{\mu} \log \left(\frac{\Delta y + r_{20}}{\Delta y + r_{10}} \right) \right]_{y'=-b}^{y'=b}, \quad (31)$$

$$v = -\frac{p}{4\pi} \left[\frac{1}{\lambda + \mu} (K_2 - K_1) + \frac{z}{\mu} \log \left(\frac{\Delta x + r_{02}}{\Delta x + r_{01}} \right) \right]_{x'=-a}^{x'=a}, \quad (32)$$

in which

$$J_j = \Delta y \left[\log(z + r_{j0}) - 1 \right] + z \log \left(\frac{1 + \psi_{j0}}{1 - \psi_{j0}} \right) + 2|a \mp x| \tan^{-1} \left(\frac{|a \mp x| \psi_{j0}}{z + \beta_{j0}} \right),$$

$$K_j = \Delta x \left[\log(z + r_{0j}) - 1 \right] + z \log \left(\frac{1 + \psi_{0j}}{1 - \psi_{0j}} \right) + 2|b \mp y| \tan^{-1} \left(\frac{|b \mp y| \psi_{0j}}{z + \beta_{0j}} \right),$$

The vertical displacements are given by:

$$w = -\frac{p}{4\pi\mu} \left[\frac{\lambda + 2\mu}{\lambda + \mu} (L_1 - L_2) + z \left\{ \tan^{-1} \frac{(a-x)\Delta y}{zr_{10}} + \tan^{-1} \frac{(a+x)\Delta Y}{zr_{20}} \right\} \right]_{y'=-b}^{y'=b}, \quad (33)$$

or

$$w = -\frac{p}{4\pi\mu} \left[\frac{\lambda + 2\mu}{\lambda + \mu} (M_1 - M_2) + z \left\{ \tan^{-1} \frac{(b-x)\Delta x}{zr_{01}} + \tan^{-1} \frac{(b+x)\Delta x}{zr_{02}} \right\} \right]_{x'=-a}^{x'=a}, \quad (34)$$

in which

$$L_j = \Delta y \left[\log(\pm a - x + r_{j0}) - 1 \right] + (\pm a - x) \log \left(\frac{1 + \psi_{j0}}{1 - \psi_{j0}} \right) + 2z \tan^{-1} \left[\frac{z\psi_{j0}}{(\mp a - x) + \beta_{j0}} \right],$$

$$M_j = \Delta x \left[\log(\pm b - y + r_{0j}) - 1 \right] + (\pm b - y) \log \left(\frac{1 + \psi_{0j}}{1 - \psi_{0j}} \right) + 2z \tan^{-1} \left[\frac{z\psi_{0j}}{(\mp b - y) + \beta_{0j}} \right],$$

The results of the obtained displacement field are given below together with the strain and pressure field. The figures contain 3D representations and cross-sections to accurately compare the numerical model with the analytical solution provided by Becker et al (2004). First, two profiles with points confined to the surface of the half space and perpendicular to each other were analysed (figure 9). For both u & v (horizontal displacements) and for w (vertical displacements) a plot could be made to analyse and compare the displacements computed by the numerical model and the analytical equations. The horizontal components of displacement (u and v) for both computations of profile 1 are shown in figure 10a. Equivalently, the results for profile 2 are shown in figure 11a. The vertical displacements (w) for both profiles are represented in figures 10b and 11b respectively. The set of curves for both FEM and the analytical expressions in each figure show identical features and values especially in high resolution.

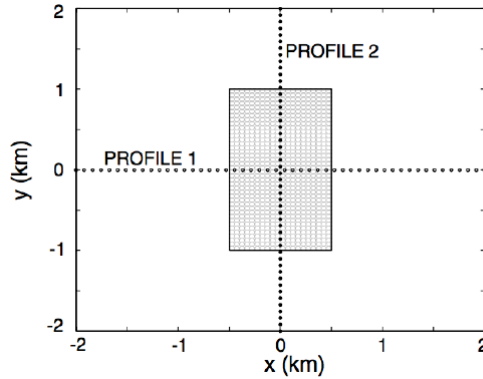
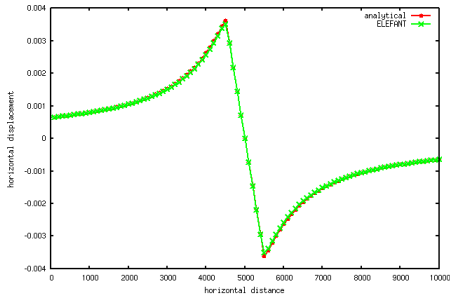
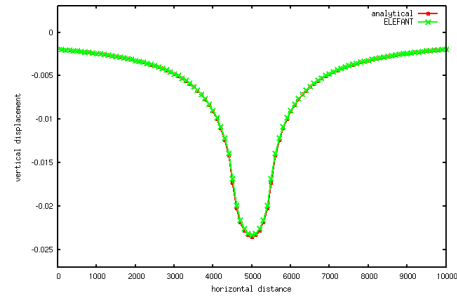


Figure 9: Cross-sections with profile 1 along the x-axis and profile 2 along the y-axis

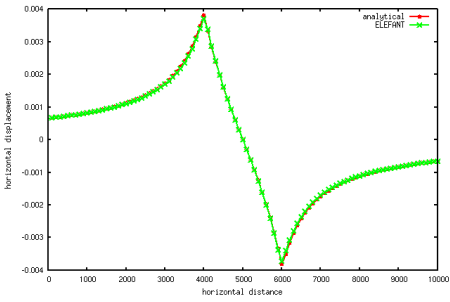


(a) Horizontal displacement along x-axis

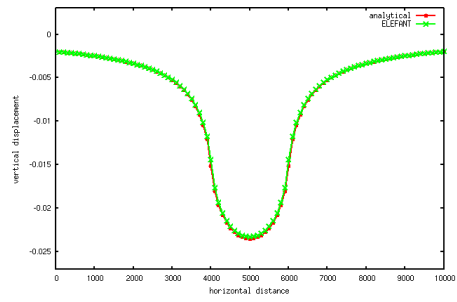


(b) Vertical displacement along x-axis

Figure 10: Cross-section profile 1



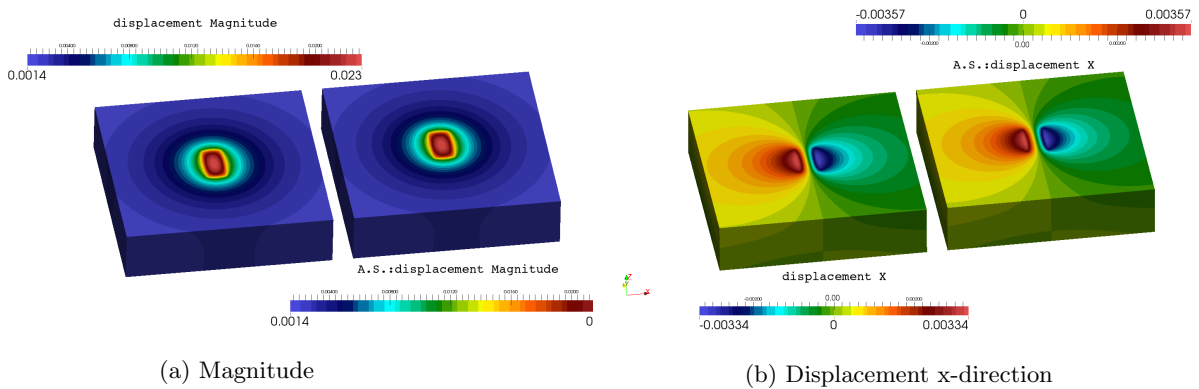
(a) Horizontal displacement along $x=Lx/2$ line



(b) Vertical displacement along $x=Lx/2$ line

Figure 11: Cross-section profile 2

The 3D representations in figures 12 & 13 again show (nearly) identical values or colours for the displacements in the horizontal directions u & v and the vertical direction w when a high resolution mesh is used. This will minimize the errors and therefore the plots are identical when observing from a distance. A detailed error analysis will be executed in the next paragraph to see if resolution changes acts linearly on the errors as we would expect in a linear finite element model. The pressure and effective strain values are given in figure 13. The pressure is of the same magnitude as the applied pressure, only slightly less. The small amounts of strain can be explained using Hooke's law in paragraph 2.1.2.



(a) Magnitude

(b) Displacement x-direction

Figure 12: Computed displacements and analytical solution (magnitude & X)

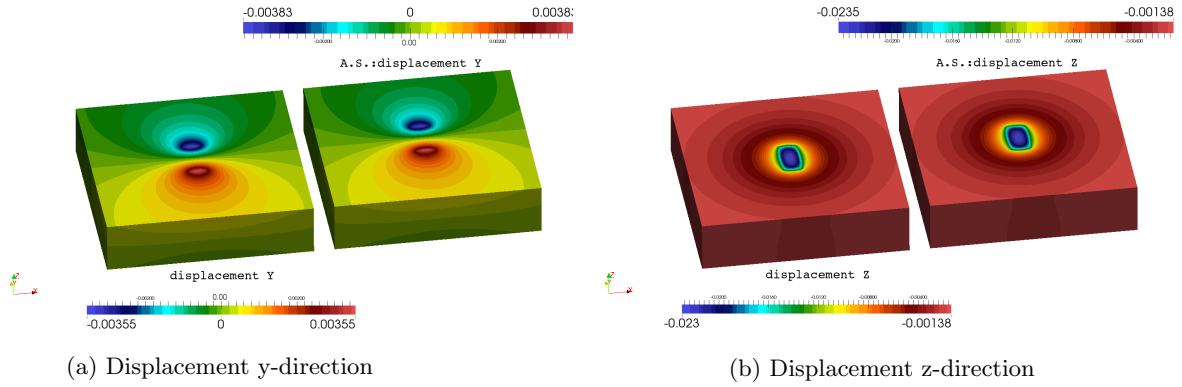


Figure 13: Computed displacements and analytical solution (Y & Z)

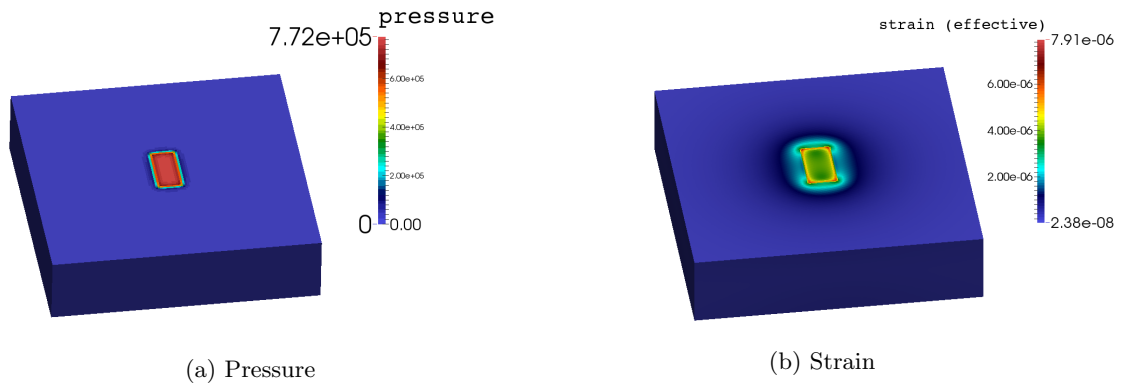


Figure 14: Pressure & strain under applied load

3.3.2 Error Analysis

The error analysis of this contact problem consist of two individual tests. In figure 15 the errors are plotted with increasing resolution, or smaller element size, to the bottom left corner. The errors are computed by simply subtracting the theoretical value for the displacement from the numerical value computed for the displacement. A logarithmic scale is used as the element size also decreases logarithmically. The fit in the plots show trends that are similar in all three directions. The slopes of the curve-fits are very close to the expected value of 1, or -1 when increasing resolution, representing a clear linear relation. The computed errors show some deviations for a number of grid sizes, especially for the x- and y-direction displacements.

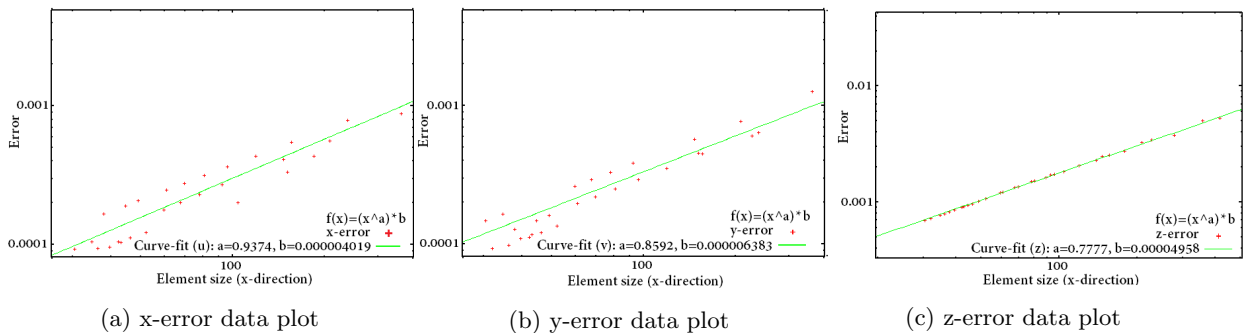


Figure 15: Error plots of displacement in the direction u , v and w

To decrease this effect a L^2 Norm error analysis is executed. The following equations are used to compute the discretisation errors for the displacements:

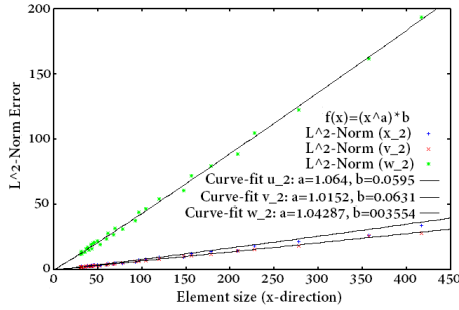
$$e_{L_2}^u = \sqrt{\int_{\Omega} (u^{th} - u)^2 dV} = \sqrt{\sum_{iel=1}^{nel} \int_{\Omega_{iel}} (u^{th} - u)^2 dV} \quad (35)$$

$$e_{L_2}^v = \sqrt{\int_{\Omega} (v^{th} - v)^2 dV} = \sqrt{\sum_{iel=1}^{nel} \int_{\Omega_{iel}} (v^{th} - v)^2 dV} \quad (36)$$

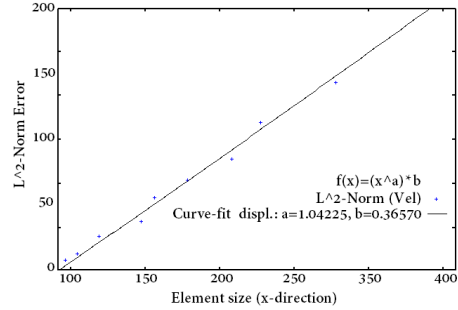
$$e_{L_2}^w = \sqrt{\int_{\Omega} (w^{th} - w)^2 dV} = \sqrt{\sum_{iel=1}^{nel} \int_{\Omega_{iel}} (w^{th} - w)^2 dV} \quad (37)$$

$$e_{L_2}^{dspl} = \sqrt{\int_{\Omega} [(u^{th} - u)^2 + (v^{th} - v)^2 + (w^{th} - w)^2] dV} = \sqrt{\sum_{iel=1}^{nel} \int_{\Omega_{iel}} [(u^{th} - u)^2 + (v^{th} - v)^2 + (w^{th} - w)^2] dV} \quad (38)$$

Equations 40, 41 and 42 compute the discretisation errors of the displacements for the three directions (u , v and w). The equations take the square roots of the sum of the absolute displacement values squared. The plots of the errors computed by equations 40-42 can be found in figure 16a and show a similar linear result as in figure 15 but much smaller deviations for all displacement directions and the high resolution models show very small error for all directions. Equation 43 is plotted in figure 16b and computes the sum of all mean squared displacements. Again a linear decline in the errors can be obtained when increasing the resolution. The highest resolution test (324x324x81 elements) contained a combined error of only 15, which means for each individual element on average an error of 1.76e-6.



(a) Combined u , v and w direction



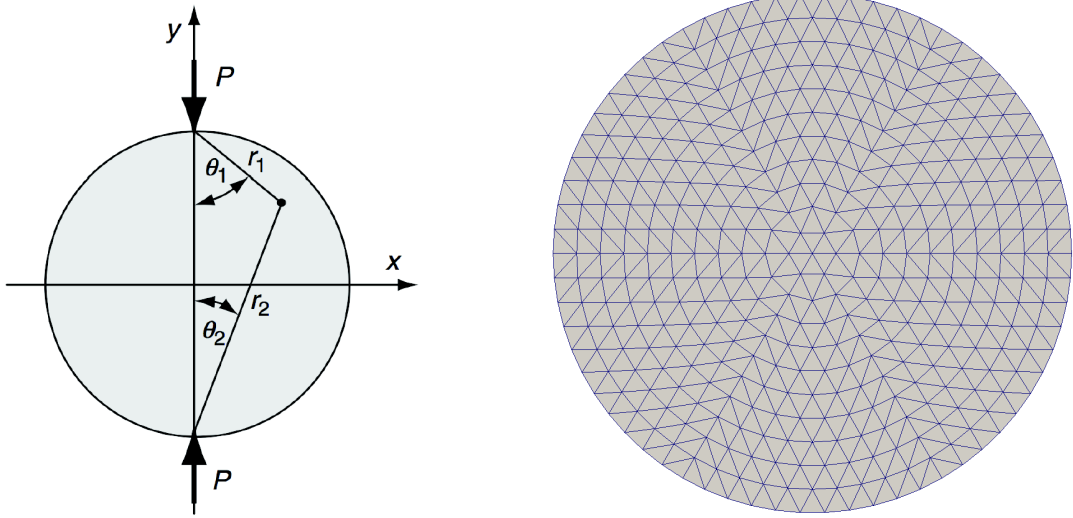
(b) Root mean square error of the displacements

Figure 16: L^2 -Norm error plots of the displacements

3.4 Point load on a Disc (2D)

To investigate the stress behavior within a sphere under two opposite but equal concentrated loads Flamant's theory (Flamant, 1892) can be used. Flamant's problem describes the stresses resulting from a point force system acting at the origin of a half-space (Sadd, 2009) and is a modification of the 3D model obtained by Boussinesq. The displacements however in this 2D model by Flamant contain unbounded logarithmic effects which lead to unrealistic values at infinity so it can not be used to describe the total displacement field. This indirect tension test, to determine the tensile stresses along a loaded diameter, will provide a valuable description of the materials strength as regular or direct tension tests have shown difficulty in determining the far-field stresses.

To solve this problem for a point load on a sphere, or actually two equal but opposite forces, a superposition scheme is used (Sadd, 2009). To obtain this total stress distribution solution two Flamant's solutions providing the stress behaviours at the boundaries are used together with a radial tension loading removing all boundary tractions which were initially created by the point forces at the surface. So three stress solutions together create the complete stress solution in a sphere. Figure 17a explains the input values schematically and figure 17b shows the grid type used for this experiment with its discretisation (resolution) by the number of layers ($nlayers$), from the centre of the sphere to the surface, as a variable in the FEM code. The radius of the sphere is set to 1, μ is set to 1 and ν is set to 0.25. The boundary conditions are set for the top and bottom of the sphere at $r = R$ and $r = -R$ where the point forces are applied. The number of layers should be an odd number to create a symmetrical grid with pressure applied exactly at $x=0$ and therefore at the center of an element's segment. The horizontal displacement and all displacements at the center of the sphere are set to zero.



(a) 2D Disk under two equal forces P with radii r_1 & r_2

(b) Grid type -19 (FEM)

Figure 17: Schematic representation of the disc under load

The final analytical stress solution after the removal of the boundary tractions is given by:

$$\sigma_x(x, z) = -\frac{2P}{\pi} \left[\frac{(R-y)x^2}{r_1^4} + \frac{(R+y)x^2}{r_2^4} - \frac{1}{D} \right] \quad (39)$$

$$\sigma_z(x, z) = -\frac{2P}{\pi} \left[\frac{(R-y)^3}{r_1^4} + \frac{(R+y)^3}{r_2^4} - \frac{1}{D} \right] \quad (40)$$

$$\sigma_{xz}(x, z) = \frac{2P}{\pi} \left[\frac{(R-y)^2x}{r_1^4} - \frac{(R+y)^2x}{r_2^4} - \frac{1}{D} \right] \quad (41)$$

with

$$r_1 = \sqrt{x^2 + (R - y)^2} \quad r_2 = \sqrt{x^2 + (R + y)^2}$$

The pressure is given by:

$$\begin{aligned} p(x, 0) &= -\frac{1}{2}(\sigma_x + \sigma_z) \\ &= \frac{P}{\pi} \left[\frac{(R - y)x^2}{r_1^4} + \frac{(R + y)x^2}{r_2^4} - \frac{1}{D} \right] + \frac{p}{\pi} \left[\frac{(R - y)^3}{r_1^4} + \frac{(R + y)^3}{r_2^4} - \frac{1}{D} \right] \\ &= \frac{P}{\pi} \left[\frac{(R - y)x^2 + (R - y)^3}{r_1^4} + \frac{(R + y)x^2 + (R + y)^3}{r_2^4} - \frac{2}{D} \right] \end{aligned} \quad (42)$$

For $z=0$ (on the x -axis), the simplified results are:

$$\sigma_x(x, 0) = \frac{2P}{\pi D} \left(\frac{D^2 - 4x^2}{D^2 + 4x^2} \right)^2 \quad (43)$$

$$\sigma_z(x, 0) = -\frac{2P}{\pi D} \left(\frac{4D^4}{(D^2 + 4x^2)^2} - 1 \right), \quad (44)$$

$$\sigma_{xz}(x, 0) = 0 \quad (45)$$

$$\begin{aligned} p(x, 0) &= \frac{P}{\pi} \left[\frac{(R - y)x^2 + (R - y)^3}{r_1^4} + \frac{(R + y)x^2 + (R + y)^3}{r_2^4} - \frac{2}{D} \right] \\ &= \frac{P}{\pi} \left[\frac{Rx^2 + R^3}{(x^2 + R^2)^2} + \frac{Rx^2 + R^3}{(x^2 + R^2)^2} - \frac{2}{D} \right] \\ &= \frac{2P}{\pi} \left[\frac{R(x^2 + R^2)}{(x^2 + R^2)^2} - \frac{1}{D} \right] \\ &= \frac{2P}{\pi} \left[\frac{R}{(x^2 + R^2)} - \frac{1}{D} \right] \end{aligned} \quad (46)$$

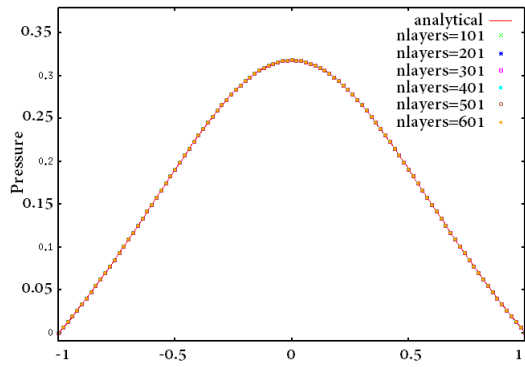
For $x=0$ (on the z -axis), the simplified results are:

$$\sigma_x(0, z) = \frac{2P}{\pi D} \quad (47)$$

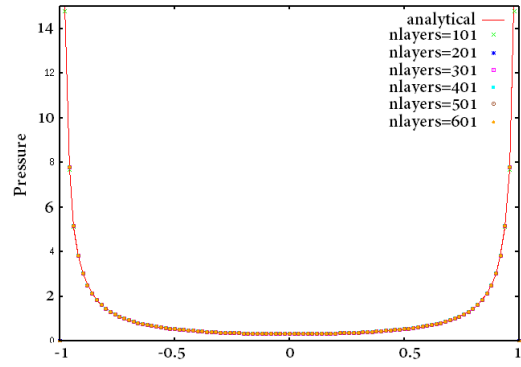
$$\begin{aligned} \sigma_z(0, z) &= -\frac{2P}{\pi} \left(\frac{2}{D - 2y} + \frac{2}{D + 2y} - \frac{1}{D} \right), \\ &= -\frac{2P}{\pi} \left(\frac{1}{R - y} + \frac{1}{R + y} - \frac{1}{D} \right), \end{aligned} \quad (48)$$

$$\sigma_{xz}(0, z) = 0 \quad (49)$$

$$\begin{aligned} p(0, z) &= \frac{P}{\pi} \left[\frac{(R - y)^3}{(R - y)^4} + \frac{(R + y)^3}{(R + y)^4} - \frac{2}{D} \right] \\ &= \frac{P}{\pi} \left[\frac{1}{R - y} + \frac{1}{R + y} - \frac{2}{D} \right] \end{aligned} \quad (50)$$

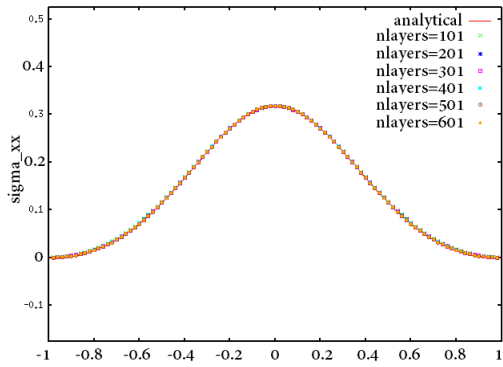


(a) pressure along x-axis

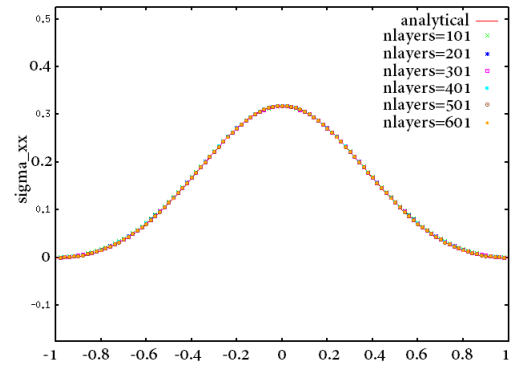


(b) pressure along z-axis

Figure 18: Cross-sections of pressures through the sphere's center and parallel to both the x- & z-axis

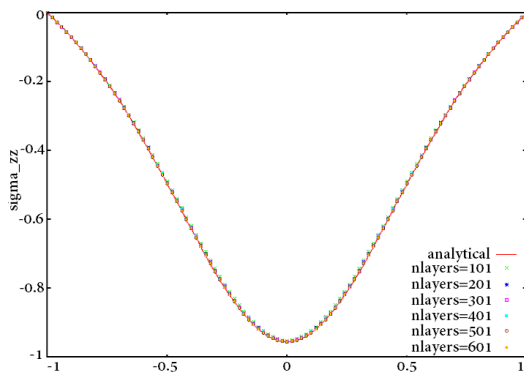


(a) σ_{xx} along the x-axis

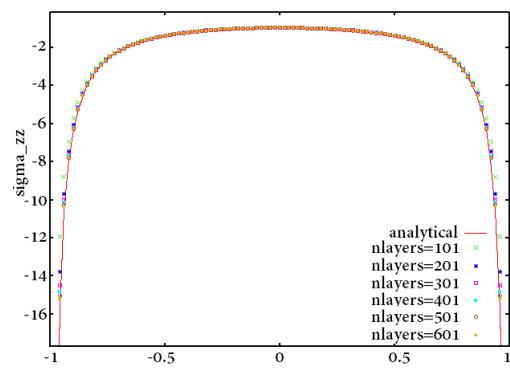


(b) σ_{xx} along the z-axis

Figure 19: Cross-sections of σ_{xx} through the sphere's center and parallel to both the x- & z-axis



(a) σ_{zz} along the x-axis



(b) σ_{zz} along the z-axis

Figure 20: Cross-sections of σ_{zz} through the sphere's center and parallel to both the x- & z-axis

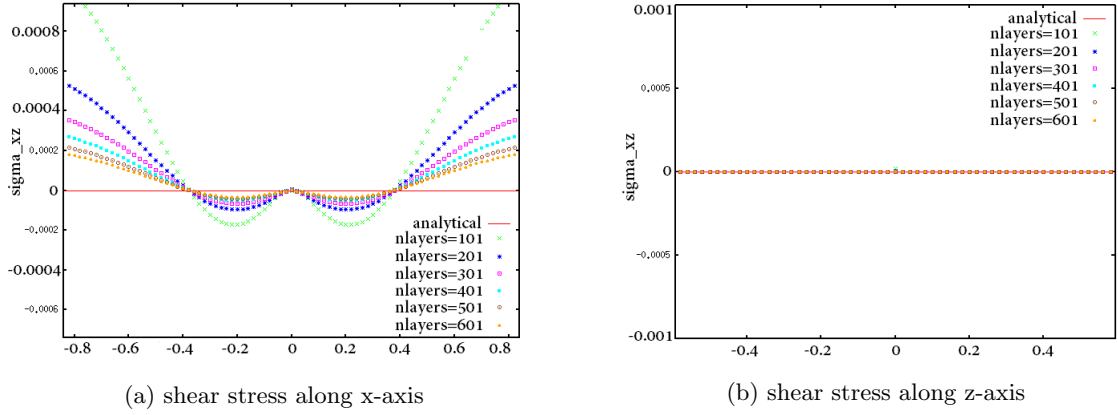


Figure 21: Cross-sections of σ_{xz} through the sphere's center and parallel to both the x- & z-axis

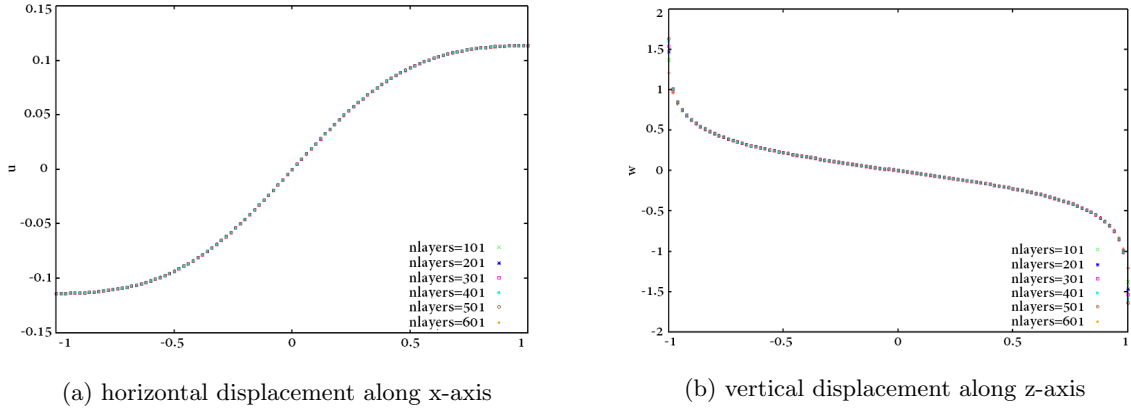


Figure 22: Cross-sections of the displacements

Figure 18-22 represent all profiles through the centre of the sphere in terms of pressure, stress and displacement. The analytical solution is plotted together with the numerical solution for different discretisations. All plots show identical values for all discretisations in the numerical model and for the analytical solution. The curves in 18a, 19a and 20a for respectively the pressure, σ_{xx} and σ_{zz} parallel to the x-axis are perfectly symmetrical which is expected as both applied forces are identical. The pressure along the z-axis (figure 18b) is nearly zero at the centre and takes rather large values close the contact areas where the forces are applied ($z=-1$ & $z=1$). The analytically computed principle stress σ_{zz} along the z-axis is constant through the sphere as can be seen in figure 20b, the numerically obtained stresses become singular close to contact area. When increasing the resolution (nlayers=601) this effect decreases and accurate magnitudes of stresses are obtained in the vicinity of the contact area. The shear stress along the x-axis in figure 21a shows the same effect, the higher resolution (orange curve) is in best agreement with the analytical stress value 0. Notice the stretched y-axis for this analysis to clearly present this effect. Nonetheless, for all resolutions the errors are negligible small. The displacements along the x- and z-axis are presented in figure 22. As explained earlier, no 2D analytical solution exist for this problem due to unbounded logarithmic effects. The displacements are however found to be reliable as the values are identical for all discretisations. The curves also represent the expected values for the displacement, 0 at the centre of the sphere for both axis and from -0.11 to 0.11 and 1.6 to -1.6 for the x-axis and z-axis respectively.

The next series of figures show the pressure - and stress distributions for both the FEM as the analytical solutions. The displacements obtained by the numerical model are also shown for both axis.

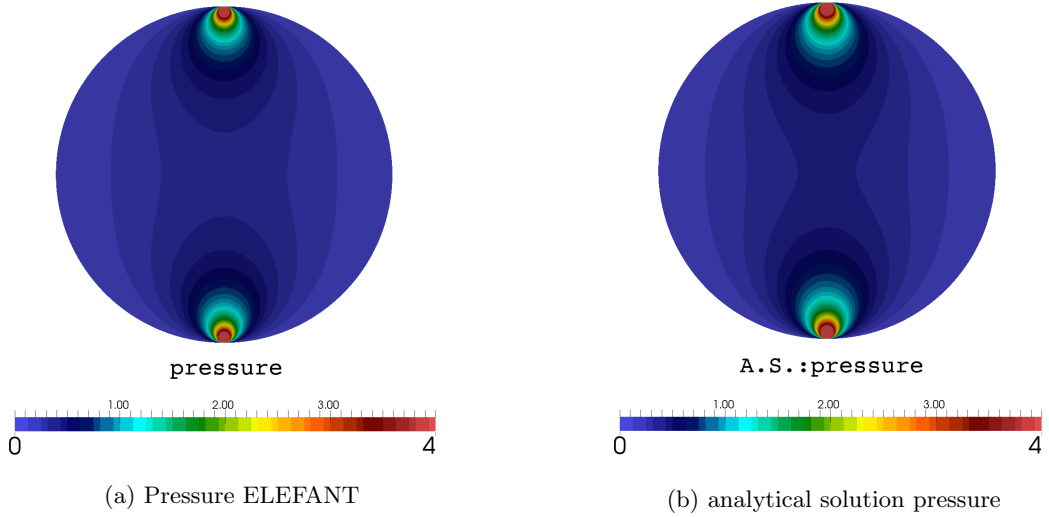


Figure 23: Pressure

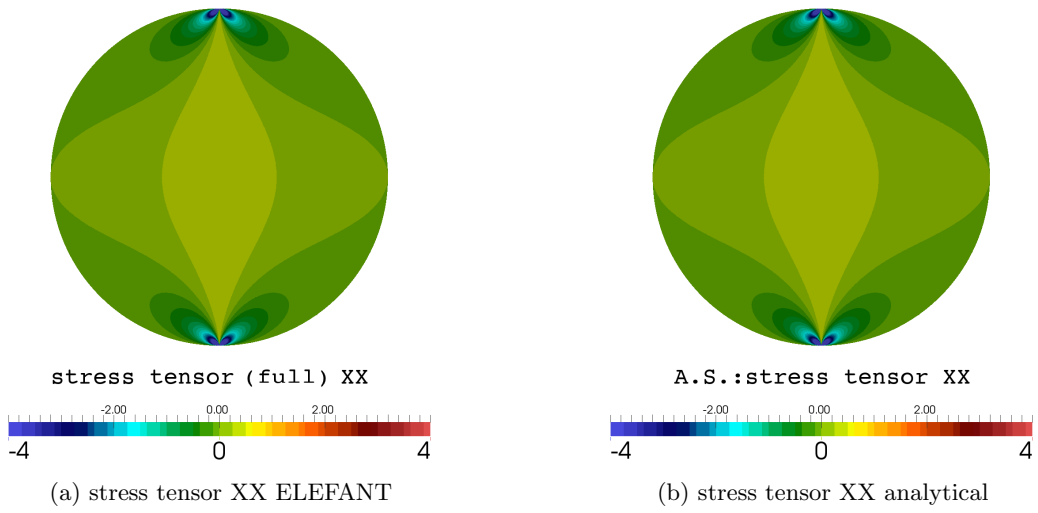


Figure 24: Stress tensor (full) σ_{xx}

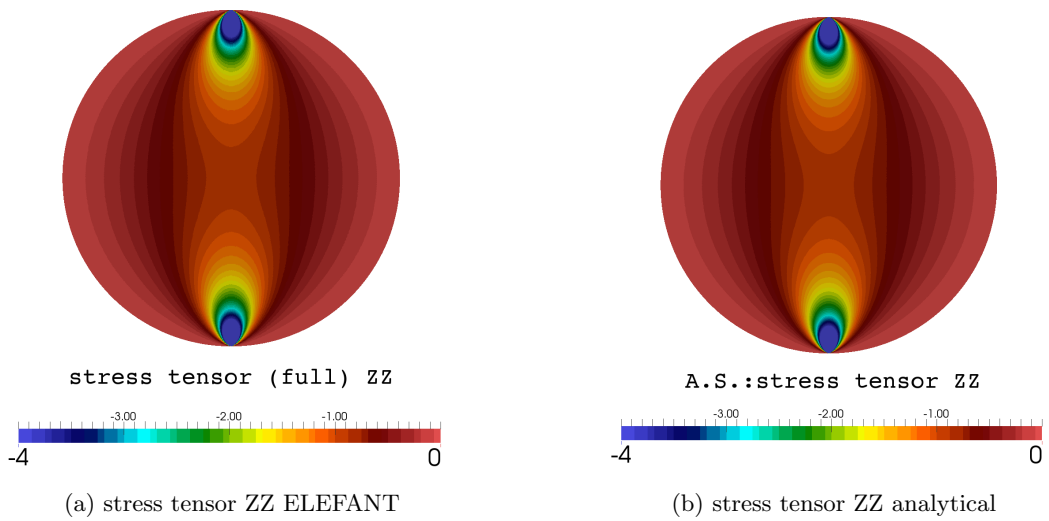


Figure 25: Stress tensor (full) σ_{zz}

For accurately comparing the differences between the numerical model and the analytical solution the data ranges are kept similar instead of automatically rescaling to fit for each individual data range. Analysing figure 23, the FEM measured pressures are identical to the analytically obtained pressures near the contact areas as was already noticed in figure 18b. However, the pressures some distance away from contact area and close to the center of the sphere show some minor deviations. With this discrete colour scheme slightly higher values for pressure are noticeable for the analytical solution for pressure. Similar deviations are noticeable for the shear stress distributions (figure 28ab). For the horizontal- and vertical stress distributions this effect does not occur (figure 24ab, 25ab & 26ab). High resolution tests have been conducted to eliminate this effect but the cause for these discrepancies is not the discretisation by the number of layers but due to properties of the chosen element type. The displacements are shown in figure 27. Along the loaded diameter ($x=0$) the tensile stresses are given by equation 52. Knowing the sample size and the amount of loading will allow the determination of the material's strength.

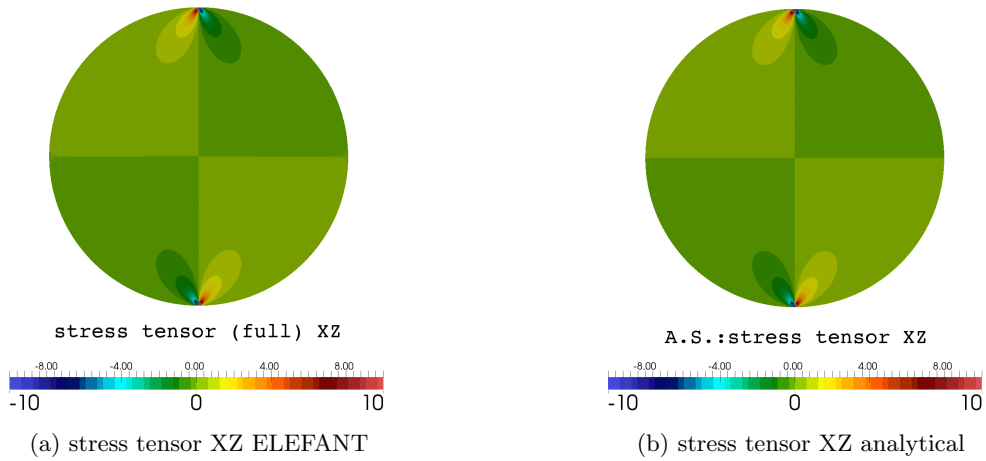


Figure 26: Stress tensor (full) σ_{xz}

Zero displacements are found at the center of the sphere and gradually increasing values are found from the center towards the contact areas (figure 27a). For the horizontal displacement, a gradual increase is visible to both sides along the x-axis starting with zero displacement at the center creating tensional stresses within the sphere. Near the contact area, just outside the loading point, the displacements are inverted creating compressional stresses towards the loading point. The vertical displacement is characterized by two oppositely orientated displacements gradually decreasing towards the center of the sphere. These magnitudes are similar to the total magnitude (figure 27a) as the horizontal displacements only has a minor contribution to the total displacement.

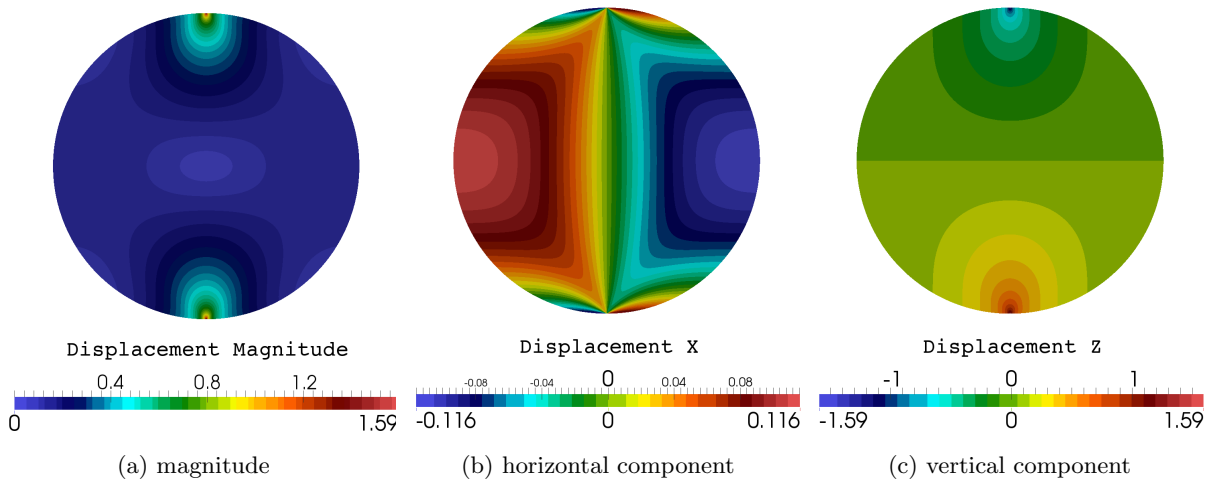


Figure 27: Displacements computed by ELEFANT

The shear components modelled by ELEFANT are visible in figure 28. As mentioned before a small deviation is noticeable near the center of the sphere. Another theoretical contours representation of the maximum shear stress together with a photo-elastic contours representation (figure 29) are available in Sadd (2009). Similar patterns are visible and the numerical/theoretical results match very well except for the regions near the contact area. This is caused by the load applied in the photo-elastic test which was a little more distributed over the area resulting in a maximum shear stress just below the contact area. This pattern also occurred when loading a semi-infinite half space under a uniform strip load (example 8.4.9 from Sadd, 2009). Maximum shear stress τ_{max} takes a maximum value at depth a (loading area = $2 \times a$), so just below the sphere's surface. Initial material failure is expected to occur at this location while a concentrated load expresses a singular amount of stress at the surface gradually decreasing towards the center of the sphere.

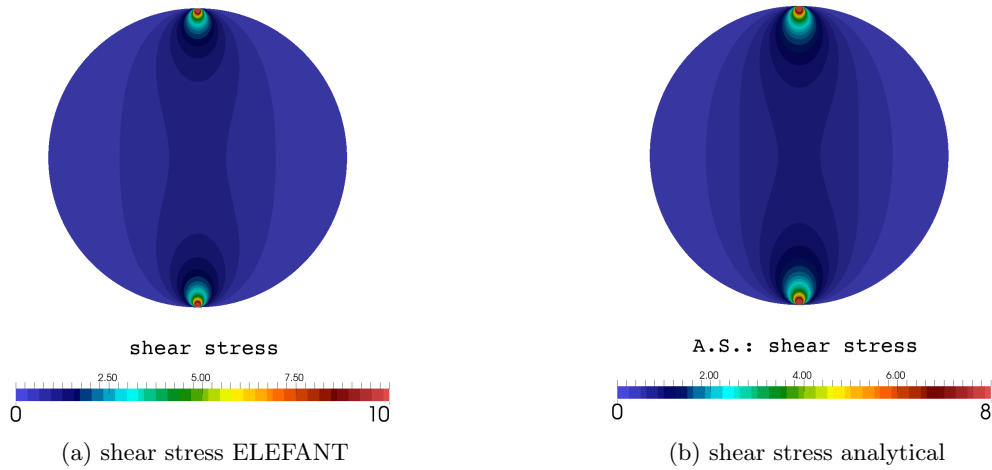


Figure 28: Shear stress

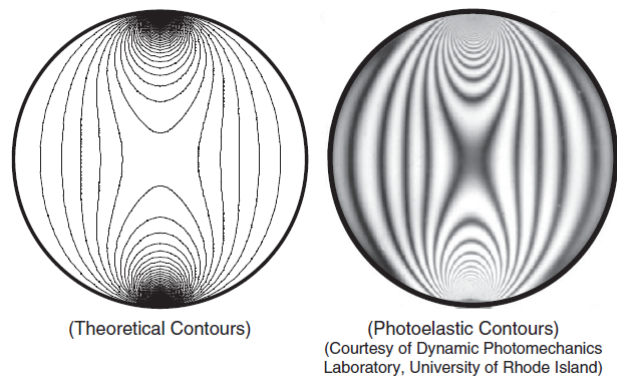


Figure 29: Theoretical and photo-elastic contours of shear stresses (Sadd, 2009)

4 Outlook & Discussion

4.1 Basic packing model

In the previous section a number of experiments have been conducted in order to test the finite element model ELEFANT for simple stresses and displacements in homogeneous and isotropic elastic bodies with different dimensions and shape. The final experiment, of a disk under two concentrated loads, is crucial for the micromechanical analysis of failure development in sandstones. Stresses & strains in these models can give great insight in potential failure sites within individual grains that will lead to macromechanical failure in for instance reservoir rocks. To use this numerical model in these perspectives multiple disks should be used to display the stress-, strain- and displacement field interacting with each other. A simple cubic packing configuration will be straightforward in terms of stresses while a hexagonal packing or rotated (45°) cubic packing will also involve shear components between the individual grains (figure 30). Notice the porosity difference between a cubic packing system and the hexagonal packing system. In addition, a hexagonal packing system can be subjected to higher stresses as they are equally transmitted through all single contact points increasing the maximum applicable applied force before grain failure will occur. The expected crack types and their evolution are closely related to these stress locations as was shown in the experiments by Dik (2016) & Cals (2017). To predict the occurrence of potential failure sites, the results from different executed compression tests and existing theories like the Hertzian contact theory can be compared to the benchmarked Finite Element Model ELEFANT. In addition, mathematical solutions for surface stresses have been obtained to test the accuracy of the Hertzian contact theory. Two tensile stress areas and one shear stress area can be located in the models: i) the maximum tensile stress at the contact area, ii) the maximum tensile stress on the z-axis beneath the contact area and iii) the maximum shear stress along the z-axis (Hertz-Huber analysis). The locations are probably the initiation sites of mode I cracks which are particularly responsible for grain failure.

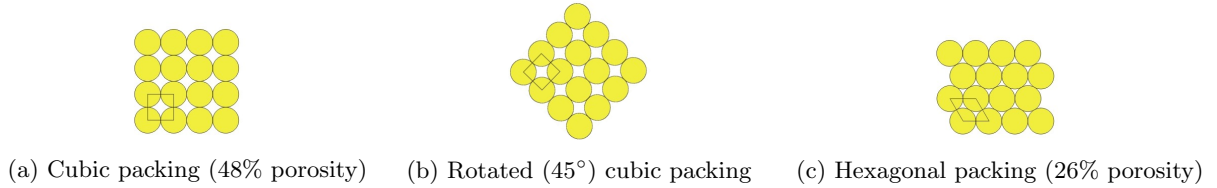


Figure 30: Packing configurations with point loading at the contacts

In addition, these crack developments are also strongly effected by flattened contact areas, or higher coordination numbers, as it results in significantly smaller stresses both at the sphere's outer surface, due to pressure distribution over a larger area, but also within the sphere (Wu and Chau, 2005). Also lower porosity's are expected with increasing flattening. The location of the maximum stresses for flattened contact area's is found to be just beneath the contact area when applying a uniform strip load (figure 31). Wu et al (2005) obtained an analytical solution for a sphere under a static compression by a uniform load which can be used to benchmark the numerical model. A point load, on the other hand, experiences maximum stresses exactly at the contact points (Sadd, 2009) (Turner et al., 2016). The isochromatic photo-elastic fringe patterns in figure 31 represent the near field maximum shear stress lines and can also be used to compare with the FEM model and determine potential failure sites for flattened sphere contacts. This location for this maximum shear stress in a flattened contact problem differs significantly from the analytical Hertzian or Boussinesq's solution which is used for point contact problems. It will especially apply for a system with irregular contact areas in terms of size or/and with even more complex, truncated or sutured, contact areas as typical sandstone grains show (Brzesowsky et al., 2014)(Cals et al., 2017).

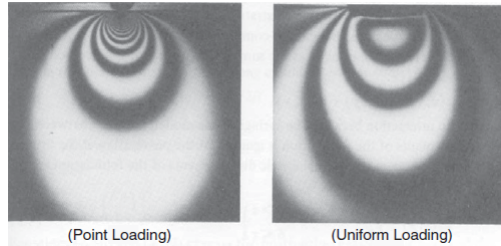


Figure 31: Photo-elastic fringe patterns for a point loading and a uniform strip load (Johnson, 1987)

4.2 Mesh refinement

To provide ELEFANT with a mesh in which the flattened contact areas can be tested a Delaunay triangulation program named Triangle is used. A Delaunay triangulation of a vertex set is a triangulation of the vertex set with no vertex in the circumference of another vertex set, meaning that all Triangle's are carefully positioned within a single sphere. High resolution is required to suppress large area differences between the different Triangles. The mesh can be adjusted with programmed switches to suppress very small angles (area constraints) within a Triangle and to classify high resolution areas required for the (near) surface regions of each individual sphere. Turner et al (2016) predicted maximum tensile stresses and their distributions through the sphere. The highest stress gradients can be found within approximately 30% of the radial distance from the surface so these areas are triangulated in higher resolution. The size of the system can be adapted in both x- and z-direction. The program Triangle requires an input of vertices and its connectivity to start a Delaunay triangulation. The input of vertices is computed by the code *optres.f90* and can be found in appendix C together with its flowchart and the geometry calculations to provide each vertex with its specific coordinates. The program additionally requires an input from the user for the radius of each individual sphere, the element size (spacing between each vortex on the outer shells) and the length (L) of the total system. This length can be adjusted to change the size of the contact area.

The program *optres.f90* writes a *.poly* file which can be read by Triangle to form the triangulation. The refinement switch (r) and the area constraint ($q33$ =minimum angle of 33°) are used to improve the quality of the final mesh. The triangulated mesh can then be visualized, refined or used to numerically model the system under loading using the finite element model ELEFANT. The generated mesh can be found in the figures below (5 by 3 spheres). Notice the flattened contact areas in figure 32 and 33b, the contact area can be increased to compare stress distributions for different contact areas and to investigate the effect of porosity reduction. The high resolution at the sphere's surface and near the pore-space is clearly visible in figure 32a:

4.3 Discussion

The Hertzian contact theory has been used in many experiments addressing the cause of sandstone failure. It has given satisfactory results in experiments focussing on surface tensile stress distributions which is believed to be the main initiation area of grain failure. Finite element calculations have shown similar results for the near field solution by Hertz but an accurate solution for the far field stresses was only described by Sternberg & Rosenthal (1952) and later Lurje (1963). To accurately determine the state of stress and potential failure sites a complete stress solution must be used to benchmark the numerical model as minor deviations can have impact on crack initiation and propagation. Sadd (2009) obtained a solution for the complete stress field within an individual sphere, unfortunately no complete 2D solution exists for a sphere under a uniform distributed load which would represent a flattened contact area. Flattened contact areas are very common in reservoir rocks, many irregularities occur on single grains so point loads are rarely responsible for stress distributions within individual grains. Hiramatsu et al (1966) tested whether stress patterns in an irregular test piece showed the same photo-elastic fringe patterns as within a regular sphere. The obtained fringe patterns are much the same in the vicinity of the loading axis, so within the accuracy of photo-elasticity testing the stress state of an irregular test

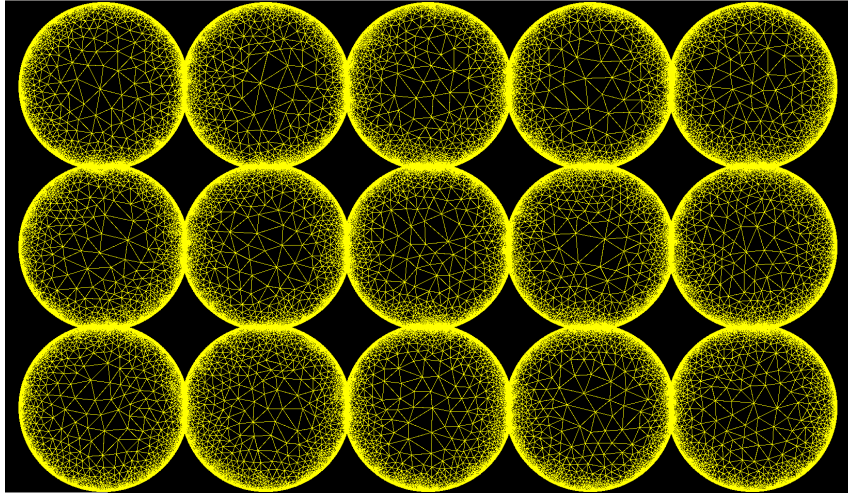
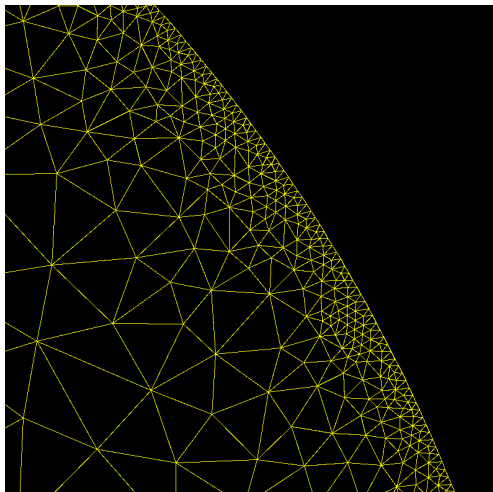
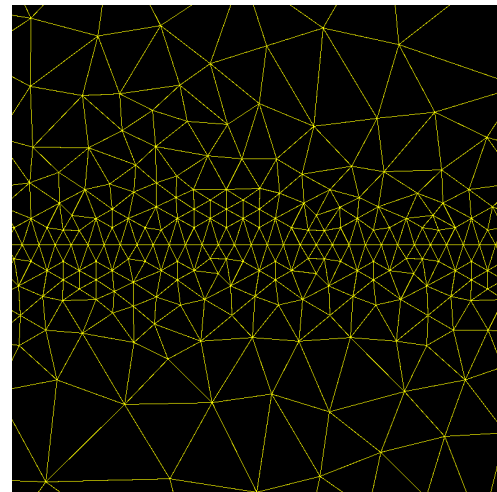


Figure 32: Optres.f90 by Delaunay Triangulation using Triangle



(a) outer boundary



(b) sphere-to sphere contact

Figure 33: Delaunay triangulation of sphere boundaries

pieces could be simplified to a regular sphere for which an analytical solution exists. The problem of a more uniformly distributed load, as is expected when two irregular grains are in contact, still exist. In addition, the stress state within the grains are also not simple and uniform (Hiramatsu and Oka, 1966). The influences of varying parameters like morphology's on the mechanical behaviour of individual grains under load is therefore necessary to precisely determine the cause of grain failure. Idealized spheres can be used to provide a reasonable indication of the magnitude of loading required to initiate grain failure but it will contain errors. Creating a bit of randomness in the model will probably help to improve the accuracy of the model.

The porosity of a reservoir rock sample inserts a significant area of concern in finite element stress modelling due the factors involved determining the final porosity (grain sphericity, roundness, grain size and packing mechanisms). Reservoirs typically have high porosity's and in general, a sandstone with a high porosity will have a lower critical crushing pressure than a low porosity sandstone (Zhang et al., 1990). The predetermined packing density in most models is a very simplified representation of an actual sandstone reservoir missing the actual randomness of pore spaces, this might result in an inaccurate stress model. Also pore pressures, exerted by for instance water or hydrocarbons, strengthen the system by reducing the effective stresses acting upon the particles. Depletion of these substances, as discussed

in the introduction, will exert important controls on production related reservoir deformation including grain failure (Brzesowsky et al., 2014). Modelling these parameters will require a triangular mesh discretised to accurately and proportionally incorporate different pore space geometry's.

This triangulation as was done using Triangle, will provide some of this randomness in the elements and can easily be adjusted to suit the needs of the problem. Brzesowsky et al (2014), Turner et al (2016) and Cho et al (2016) discussed the impact of actual grain shape on the strength of the sandstone. Natural sands have a typical range of shapes: roundness $r = 0.3 - 0.9$ and sphericity $S = 0.5 - 0.9$ which is significantly larger than for instance manufactured sands with roundness's ranging from $R = 0.2 - 0.3$ and sphericity's ranging from $S = 0.7 - 0.8$ (Cho et al., 2006). This will indeed determine the macroscale behaviour of sands to a certain extent. Besides grain size and initial porosity, grain angularity and grain size uniformity will lead to higher stress concentrations at the grain-to-grain contact (Brzesowsky et al., 2014). With the use of X-ray tomography (Turner et al., 2016) an actual grain morphology mesh was obtained for a complex geometry providing a realistic representation of individual sand grains. Again, the effect of the coordination number is noticeable. More densely packed reservoir sandstones show decreasing depths of the high stress gradients from the surface strengthen the system. So the required thickness of the high resolution shell decreases with when the coordination number increases (Turner et al., 2016).

The choice of element type is a big concern within this research. High order elements and high resolution will increase computation time while discretisations can be adjusted to the required resolution. The magnitude of computed stresses can be influence by the element chosen as by the mesh refinement. A coarser or stiffer mesh will result in an underestimation of the stresses and therefore grain failure will occur sooner than expected. So a fine mesh is required near the surface of each grain to accommodate the high stress gradient properly, a coarser mesh is sufficient some distance away from the surface but the actual location for this transition is highly dependant on typical grain angularity's. In addition, grain surface topology might change during loading. Time-dependant grain rearrangement like sliding results in a more stable less porous configuration supporting the applied load (Zhang et al., 1990). Also the change in orientation when grains start rolling and therefore the grain's angularity will effect the stress concentrations. These might also change when the applied force is not instantaneous, which is expected during the slow depletion of a gas or oil reservoir. Cracks initiation shows a time dependence as divergent cone cracks propagate away from the loading point towards the surface when compression rates are slow and convergent cone cracks occur at high compression rates (Brzesowsky, 1995). Nonetheless, maximum tensile stresses within a sphere occur at the edges of the contact area and are the main reason for surface flaws that eventually initiate whole grain failure (Brzesowsky, 1995).

Other time-dependent processes that influences stress states and therefore grain failure are cemented contact area's and pressure solution. Cemented contact areas cause smaller magnitudes of stresses to occur than uncemented areas under similar amount of applied forces. In other words, they strengthen the system. Small amounts of cement can have huge effect on this strength so when the cement is partially distributed the mean bulk volume of cement can not be used to represent the grain model. A partial distribution scheme must be used for the location of the cement or grain failure predictions might be inaccurate. Pressure solution is responsible for the accelerated material transport from contact area to pore space initiating the compaction of a sandstone by reducing the porosity and therefore changing the stress distribution (Visser et al., 2012). Finally, the chosen Poisson ratio of the material is of interest. Slightly changing this ratio will randomize the compositional properties of the reservoir.

5 Conclusions

Highly porous reservoir sandstones are highly complex systems in terms of stress distributions at the microscale. Fluids are extracted directly disturbing the stress equilibrium and increasing the effective stress on the individual sand grains. The strengths of these grains determine the elastic and inelastic deformation causing the compaction of the total system leading to irrecoverable subsidence of the surface. Testing the strengths of reservoir rocks by conventional laboratory methods are not standard procedures anymore as numerical test take much less time and effort. The failure criterion of a single sand grain can be obtained by conventional methods including laboratory crushing experiments but modelling the complexity of a system incorporating the interaction of many parameters is favorable using a finite element model. To accurately predict potential failure initiation sites and failure mechanisms a complete and detailed model must be obtained in which the elastic response of a single grain or pack of grains under load is thoroughly tested and visualized. Analytical solutions for stress, strain, pressures and displacement have been used to benchmark the finite element model ELEFANT. Specifically, the computed numerical solutions have been compared with the analytical solutions. The Hertzian contact theory for the near field stress field has been used in different studies to obtain a complete stress and displacement solution for the whole sphere. The combination of the Hertzian contact theory together with the far-field solution by Sternberg & Rosenthal (1952) provided a proper description of stresses within a single perfect sphere under load. The transition area between these solutions agreed with other numerical models. So the Hertzian contact theory contains accurate expressions for the maximum tensile stress distribution near the contact area. It can therefore be used to predict crack initiation for a single sphere as conventional experiments have shown that initial fractures leading to grain failure develop near these contact areas. Under realistic loading conditions, the initiation of ring cracks can be observed. These equations can be used to accurately predict the critical contact force required for failure (failure criterion).

To predict the failure conditions of a meso- or macroscale system a pack of multiple grains must be modeled to obtain a clear representation of intragranular tensile stresses in the different spheres. In addition, different packing systems including a rotated 45° cubic packing system and a hexagonal packing system have huge contributions in future grain failure studies as sandstones do not show a uniform packing system. A combination of these will probably be in best agreement with actual sandstone reservoirs. Also grain radii do diverge in size, complicating the packing mechanism's even more as smaller grains fill up pore spaces to a certain extent. Contact areas between grains are also quite different in size as no individual grains of perfect sphericity exist in sandstone unless manufactured. Flattened contact areas show significantly smaller maximum stresses as they are distributed more equally over the area. On the other hand, high angularity's in individual grains could show amounts of stresses similar to magnitudes obtained in point load computations obviously increasing the chances of failure. Finally, the effect of cemented grain contacts or pressure solution, which are very common in reservoir conditions, should be implemented in future study's. They can significantly strengthen (cement) or weaken (pressure solution) the system and should be partially addressed because distributing the bulk volume of those phenomena will result in different magnitudes of effective stresses. Randomizing different parameters of diverging scale will therefore be of great importance in the finite element modelling of reservoir loading problems. Despite these many factors contributing to the stress distributing within pack of grains, the Finite Element model ELEFANT is certainly successful in modelling stresses, strains and displacements within a single spherical grain with great accuracy. To give insight into the micromechanics including grain failure of a macro-scale system the elastic behaviour within an individual grain must be properly known, so ELEFANT definitely offers potential to be used for grain-scale stress distribution modelling.

References

- Becker, J. and Bevis, M. (2004). Love's problem.
- Bernabé, Y., Fryer, D., and Hayes, J. (1992). The effect of cement on the strength of granular rocks.
- Boussinesq, J. (1885). Application des potentiels a l'étude de l'équilibre et du mouvement des solides élastiques.
- Brzesosky, R., Spiers, C., Peach, C., and Hangx, S. (2011). Failure behavior of single sand grains: Theory versus experiment.
- Brzesowsky, R. (1995). Micromechanics of sand grain failure and sand compaction.
- Brzesowsky, R., Spiers, C., Peach, C., and Hangx, S. (2014). Time-independent compaction behavior of quartz sands.
- Cals, G., Hangx, S., Peach, C., and Schimmel, M. (2017). Grain fracturing and grain re-arrangement in sands and sandstone: Studying brittle deformation features in sugar glass as an analogue.
- Cho, G.-C., Dodds, J., and Santamarina, J. (2006). Particle shape effects on packing density, stiffness, and strength: natural and crushed sands.
- Davis, R. and Selvedurai, A. (1996). *Elasticity and Geomechanics*. Cambridge University Press.
- Dik, R. (2016). Sandstone compaction by grain breakage and rearrangement: A see-through experimental study using 2-d sugar-glass grain packs as a sandstone analogue.
- Donea, J. and Huertaa, A. (2003). *Finite Element Methods for Flow Problems*. John Wiley.
- Flamant, A. (1892). Sur la répartition des pressions dans un solide rectangulaire chargé transversalement.
- Hertz, H. (1896). Miscellaneous papers by h. hertz.
- Hiramatsu, Y. and Oka, Y. (1966). Determination of the tensile strength of rock by a compression test of an irregular test piece.
- Johnson, K. (1987). *Contact Mechanics*. Cambridge University Press, Cambridge.
- Lawn, B. (1993). Fracture of brittle solids - second edition.
- Liu, C. (2009). Elastic constants determination and deformation, observation using brazilian disk geometry.
- Love, A. (1929). The stress produced in a semi-infinite solid by pressure on part of the boundary.
- Sadd, M. H. (2009). *Elasticity: Theory, Applications, and Numerics*. Elsevier Inc.
- Slaughter, W. (2001). *The linearized Theory of Elasticity*. Springer Science+Business Media, LLC.
- Suckale, J. (2009). Induced seismicity in hydrocarbon fields.
- Thieulot, C. (2014). Elefant: a user-friendly multipurpose geodynamics code.
- Timoshenko, S. and Goodier, J. (1970). *Theory of elasticity*. Int. 3rd ed., McGraw-Hill Int. Ed., Engineering Mechanics Series, London.
- Titovich, A. and Norris, A. (2012). Greens's function for symmetric loading of an elastic sphere with application to contact problems.
- Turner, A., Kim, F., Penumada, D., and Herbold, E. (2016). Meso-scale framework for modeling granular material using computed tomography.
- Visser, H., Spiers, C., Peach, C., and Hangx, S. (2012). Effects of interfacial energy on compaction creep by intergranular pressure solution: Theory vs. experiments on a rock analogue (nano₃).

- Wang, B., Chen, Y., and Wong, T. (2008). A discrete element model for the development of compaction localization in granular rocks.
- Williams, J. and Dwyer-Joyce, R. (2001). *Modern Tribology Handbook, Volume 1, Chapter 3*.
- Wong, T.-F. and Baud, P. (1999). Mechanical compaction of porous sandstone.
- Wong, T.-F. and Wu, L.-C. (1995). Tensile stress concentration and compressive failure in cemented granular material.
- Wu, S. and Chau, K. (2005). Dynamic response of an elastic sphere under diametral impacts.
- Zhang, J., Wong, T.-F., and Davis, D. (1990). Micromechanics of pressure-induced grain crushing in porous rocks.

Appendices

Appendix A

Hertz analysis (3D)

Set-up:

-the size of the contact area is small compared with the smallest radius of surface curvature near the contact area ($\frac{a}{R_r} \leq 0.2$). This ensures that the surfaces outside the contact area are approximately planar, so that the internal stress field can be calculated on the basis of a semi-infinite half space without being influenced by the proximity of the boundaries

-the loaded contact area is circular with radius a given by

$$a^3 = \frac{3FR_r}{4E}$$

-the normal stress component σ_0 at the centre of the contact area is given by:

$$\frac{3F}{2\pi a^2}$$

-The contact surface ($z=0$) normal stress distribution then is given by:

$$\sigma_{zz} = -\sigma_0 \sqrt{1 - \frac{r^2}{a^2}}$$

Stress distributions

Stress distributions in the RZ-plane

$$\frac{\sigma_{rr}}{\sigma_0} = \frac{1-2\nu}{3} \frac{a^2}{r^2} \left[1 - \left(\frac{z}{\sqrt{u}} \right)^3 \right] + \left(\frac{z}{\sqrt{u}} \right)^3 \frac{a^2 u}{u^2 + a^2 z^2} + \frac{z}{u} \left[\frac{(1-\nu)u}{a^2 + u} + (1+\nu) \frac{\sqrt{u}}{a} \arctan\left(\frac{a}{\sqrt{u}} \right) - 2 \right]$$

$$\frac{\sigma_{\vartheta\vartheta}}{\sigma_0} = -\frac{1-2\nu}{3} \frac{a^2}{r^2} \left[1 - \left(\frac{z}{\sqrt{u}} \right)^3 \right] - \frac{z}{\sqrt{u}} \left[2\nu + \frac{(1-\nu)u}{a^2 + u} - (1+\nu) \frac{\sqrt{u}}{a} \arctan\left(\frac{a}{\sqrt{u}} \right) \right]$$

$$\frac{\sigma_{zz}}{\sigma_0} = -\left(\frac{z}{\sqrt{u}} \right)^3 \frac{a^2 u}{u^2 + a^2 z^2}$$

With

$$2u = r^2 + z^2 - a^2 + \sqrt{(r^2 + z^2 - a^2)^2 + 4a^2 z^2}$$

Boundary conditions:

$$r \neq 0, \quad z \neq 0$$

Stress distributions along the z-axis

$$\frac{\sigma_{rr}}{\sigma_0} = \frac{\sigma_{\vartheta\vartheta}}{\sigma_0} = -(1+\nu) \left[1 - \frac{z}{a} \arctan\left(\frac{a}{z} \right) \right] + \frac{a^2}{2(a^2 + z^2)}$$

$$\frac{\sigma_{zz}}{\sigma_0} = -\frac{a^2}{a^2 + z^2}$$

Boundary conditions:

$$\text{Along the } z\text{-axis: } r=0, z \neq 0, \quad u = z^2$$

Stress distributions at the contact surface

Inside and on the periphery of the loaded circle

$$\frac{\sigma_{rr}}{\sigma_0} = \frac{1 - 2\nu}{3} \frac{a^2}{r^2} \left(1 - \left(\frac{\sqrt{a^2 - r^2}}{a} \right)^3 \right) - \frac{\sqrt{a^2 - r^2}}{a}$$

$$\frac{\sigma_{\vartheta\vartheta}}{\sigma_0} = -\frac{1 - 2\nu}{3} \frac{a^2}{R^2} \left(1 - \left(\frac{\sqrt{a^2 - r^2}}{a} \right)^3 \right) - 2\nu \frac{\sqrt{a^2 - r^2}}{a}$$

$$\frac{\sigma_{zz}}{\sigma_0} = -\frac{\sqrt{a^2 - r^2}}{a}$$

Boundary conditions:

$$z = 0, 0 < r \leq a, \quad u = 0$$

Outside of the loaded circle

$$\begin{aligned} \frac{\sigma_{rr}}{\sigma_0} &= -\frac{\sigma_{\vartheta\vartheta}}{\sigma_0} = \frac{1 - 2\nu}{3} \frac{a^2}{r^2} \\ \sigma_{zz} &= 0 \end{aligned}$$

Boundary conditions:

$$z = 0, r > a, \quad u = (r^2 - a^2)$$

Stress components at the origin

$$\begin{aligned} \frac{\sigma_{rr}}{\sigma_0} &= -\frac{\sigma_{\vartheta\vartheta}}{\sigma_0} = -\frac{1 + 2\nu}{2} \\ \frac{\sigma_{zz}}{\sigma_0} &= -1 \end{aligned}$$

Appendix B

Boussinesq 3D

Boussinesq-Point Load on a half-space

Set-up:

- Frictionless point load acting at the origin perpendicular to the flat surface (XY-plane) of an elastic half space
- Inside the elastic half space the principle stresses σ_1 and σ_3 remain respectively tensile and compressive

Solution (cylindrical coordinates):

$$\sigma_{rr} = \frac{F}{2\pi} \left[(1 - 2\nu) \left(\frac{1}{r^2} - \frac{z}{\rho r^2} \right) - \frac{3zr^2}{\rho^5} \right]$$

$$\sigma_{\vartheta\vartheta} = \frac{F}{2\pi} (1 - 2\nu) \left(\frac{1}{r^2} - \frac{z}{\rho r^2} - \frac{z}{\rho^3} \right)$$

$$\sigma_{zz} = -\frac{3F}{2\pi} \frac{z^3}{\rho^5}$$

Boundary conditions:

$$F = 10 - 25N$$

$$\vartheta = 0.077$$

$$p = (r^2 + z^2)$$

$$\text{For } z = 0, r \neq 0: \sigma_{zz} = 0, \sigma_{rr} = -\sigma_{\vartheta\vartheta} = \frac{(1-2\nu)F}{2\pi r^2}$$

$$\text{For } z \neq 0, r = 0: \sigma_{zz} = -\frac{3F}{2\pi z^2}, \sigma_{rr} = \sigma_{\vartheta\vartheta} = \frac{(1-2\nu)F}{4\pi z^2}$$

Boussinesq-Uniform circular load

Set-up:

- Uniform pressure p over a circular element (radius= a)
- Stress components along the z -axis are obtained using pressure P produced by point load F acting uniformly over a ring area of radius r and width dr (perpendicular to the Z -axis) using the equality $F = p2\pi r dr$. Substituting for F in equations 1-4 and integrating over the entire area (radius= a) gives:

Solution (cylindrical coordinates):

$$\sigma_{rr} = \sigma_{\vartheta\vartheta} = \frac{p}{2} \left[- (1 + 2\nu) + \frac{2z(1 + \nu)}{\sqrt{a^2 + z^2}} - \left(\frac{z}{\sqrt{a^2 + z^2}} \right)^3 \right]$$

$$\sigma_{zz} = -\frac{3F}{2\pi} \frac{z^3}{P^5}$$

Boundary conditions:

$$F = 10 - 25N$$

$$P = ?$$

$$\text{For } z = 0, r \leq a: \sigma_{rr} = \sigma_{\theta\theta} = -\frac{(1+2\nu)p}{2}, \sigma_{zz} = -p$$

$$\text{For } z = 0, r \geq 0: \sigma_{rr} = -\sigma_{\theta\theta} = \frac{(1-2\nu)F}{2\pi r^2}, \sigma_{zz} = 0$$

Appendix C

Triangle

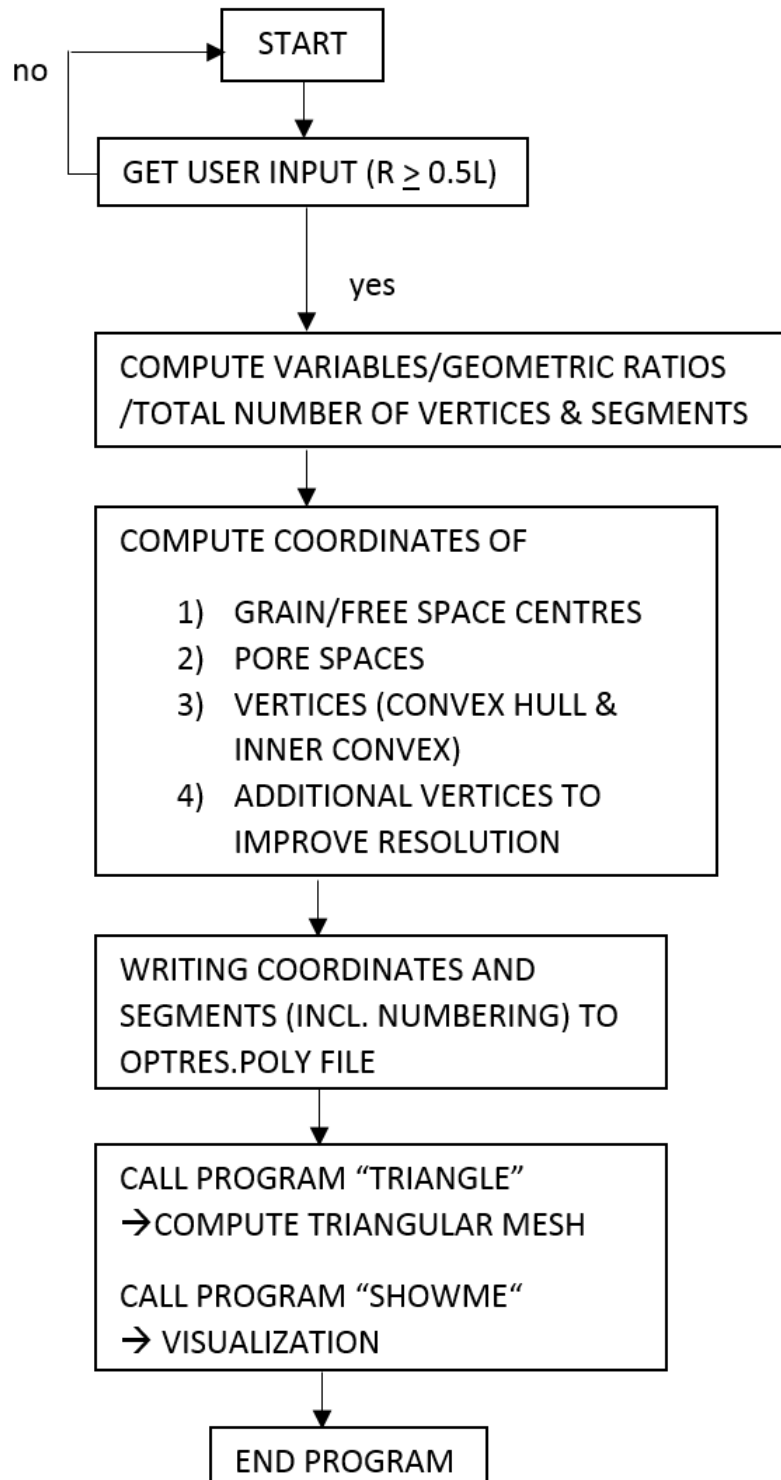


Figure 34: Flowchart of program optres.f90

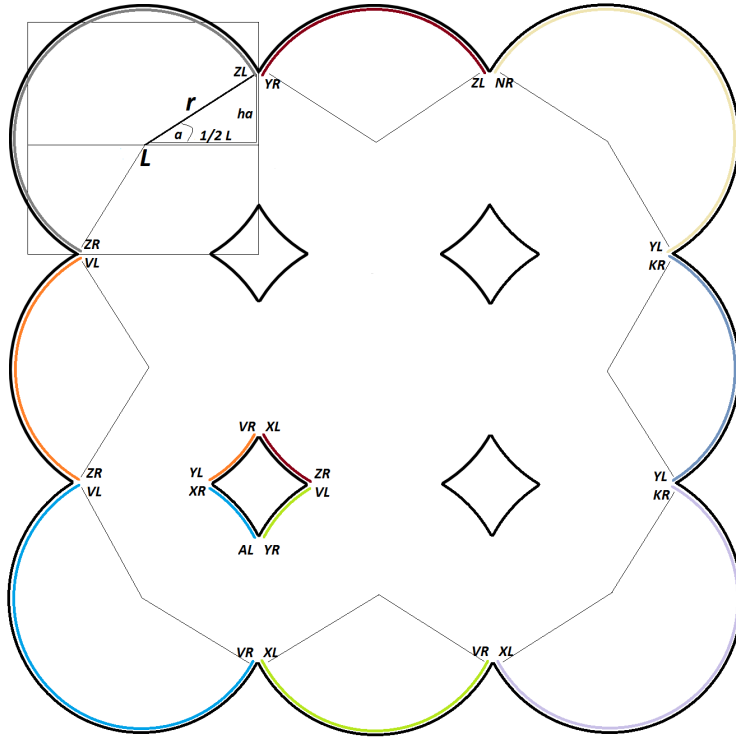


Figure 35: Geometry calculations for program optres.f90

Equations:

$$nps = (2 * pi * r / sp)$$

$$rad = (2 * pi) / nps$$

$$a = acos(0.5 * l / r)$$

$$ha = sqrt((r ** 2) - (0.5 * l) ** 2)$$

$$yl = ((1.5 * pi) + a) / (2 * pi) * nps$$

$$yr = (pi - a) / (2 * pi) * nps$$

$$zl = (a / (2 * pi)) * nps$$

$$zr = ((1.5 * pi) - a) / (2 * pi) * nps$$

$$vl = ((0.5 * pi) + a) / (2 * pi) * nps$$

$$vr = ((2 * pi) - a) / (2 * pi) * nps$$

$$xl = ((pi + a) / (2 * pi)) * nps$$

$$xr = ((0.5 * pi) - a) / (2 * pi) * nps$$

$$kr = ((2.5 * pi) - a) / (2 * pi) * nps$$

$$nr = ((3 * pi) - a) / (2 * pi) * nps$$

$$al = (a / (2 * pi)) * nps$$

$$ta = (2 * ha) / sp$$

*with sp being the space distance between each vertex on the outer shell representing the resolution. nps (or number of points) are the total number of vertices on one individual sphere.


```

!!!----- Part 1: Setup (Computing variables from input) -----!!!
!!!-----Input-----!!!
!print *, 'Enter the radius of the grains='
!read(5,*) r
!print *, 'Enter length L'
!read(5,*) L
!print *, 'Enter spacing between points'
!read(5,*) sp
!print *, 'Enter number grains X-direction'
!read(5,*) nballsx
!print *, 'Enter number grains Y-direction'
!read(5,*) nballsy

r=0.0001
L=0.000191
sp=0.0000005
nballsx=3
nballsy=3

!!!----- Variables -----!!!
total=(nballsx-1)*(nballsy-1)
pi=4.*atan(1.)
nps=(2*pi*r/sp)
rad=(2*pi)/nps

!!!----- Geometrics -----!!!
a=acos(0.5*r/r)
h=sqrt((r**2)-(0.5*r)**2)

!!!----- Ratios for convex hull segments ----!!!
vl=(0.5*pi*a)/(2*pi)*nps
vr=(2*pi)-a/(2*pi)*nps
xl=(p1*a)/(2*pi)*nps
xr=(0.5*pi)-a/(2*pi)*nps
yl=(1.5*pi*a)/(2*pi)*nps
yr=(pi-a)/(2*pi)*nps
zl=(a/(2*pi))*nps
zr=(1.5*pi)-a/(2*pi)*nps
kr=(2.5*pi)-a/(2*pi)*nps
nr=(3*pi)-a/(2*pi)*nps
al=(a/(2*pi))*nps
ta=(2*ha)/sp

!!!----- Ratios to Integers -----!!!
invl=int(vl)
invr=int(vr)
inxl=int(xl)
inxr=int(xr)
inyl=int(yl)
inyr=int(yr)
inzl=int(zl)
inzr=int(zr)
inkr=int(kr)
inlr=int(lr)
inta=int(ta)

!!!----- Total nodes mesh -----!!!
pnp=(invr-invl)*(inkr-inxl)*(inr-inyl)*(inzr-inzl) &
+((invr-inxl)*(nballsx-2))+((inkr-inyl)*(nballsy-2)) &
+((inyr-inzl)*(nballsx-2))+((inzr-invl)*(nballsy-2))
pnp=(inxr-inal)*(invr-inyl)*(inr-inxl)*(inyr-invl)
pores=(pnp*total)
spaces=(nballsx+1)*(nballsy+1)
spres=(nballsx)*(nballsy-1)
vspres=(nballsx-1)*(nballsy)
arh=(inta*spres)
arv=(inta*vspres)

!!!----- Allocating arrays -----!!!
allocate(number(pnp+pores+arh+arv))
allocate(segment(pnp))
allocate(segpores(pores))
allocate(xca(nballsx-1))
allocate(yca(nballsx-1))
allocate(xcb(nballsy-1))
allocate(ycb(nballsy-1))
allocate(xcc(nballsx-1))
allocate(ycc(nballsx-1))
allocate(xcd(nballsy-1))
allocate(ycd(nballsy-1))
allocate(xpores(pores))
allocate(ypores(pores))
allocate(xcoord(pnp))
allocate(ycoord(pnp))
allocate(spacex(spaces))
allocate(spacey(spaces))
allocate(spx(total))
allocate(spy(total))
allocate(tx(spres))
allocate(tx(spres))
allocate(ty(vspres))
allocate(vtx(vspres))
allocate(resx(arh))
allocate(resy(arh))
allocate(vresx(arv))
allocate(vresy(arv))

```

Part 1: Setup & computations from variables

```

!!!----- Part 2: Numbering & pores -----!!!
counter=0
do i=1,npnpores+nh+nv
  counter=counter+1
  number(counter)=i
end do

!!!----- Segments -----!!!
counter=0
do k=1,np-1
  counter=counter+1
  segment(counter)=k+1
  segment(np)=1
end do
counter=0
do k=np+1,np+pores-1
  counter=counter+1
  segpores(counter)=k+1
end do
do i=1,total
  counter=counter+1
  segpores(np*i)=number(((i-1)*np)+1+npnp)
end do

!!!----- Spaces (final) -----!!!
counter=0
do i=0,nballsx
  do j=0,nballsx
    counter=counter+1
    spacex(counter)=i*i
    spacey(counter)=i*i
  end do
end do
counter=0
do j=1,nballsx-1
  do i=1,nballsx-1
    counter=counter+1
    spx(counter)=i*i
    spy(counter)=j*i
  end do
end do

```

```

!!!---- Part 3: Coordinates of grain centres and inner/outer convex hull ----!!!
!!!-- Centres of grains (outer convex hull) ----!!!
counter=0
do i=1,nballelx-1
  counter=counter+1
  xca(counter)=(i*1)-(0.5*1)
  yca(counter)=(0.5*1)
end do
counter=0
do i=1,nballely-1
  counter=counter+1
  xcb(counter)=(nballelx*1)-(0.5*1)
  ycb(counter)=(i*1)-(0.5*1)
end do
counter=0
do i=0,nballelx-2
  counter=counter+1
  xcc(counter)=(nballelx*1)-(0.5*1)-(i*1)
  ycc(counter)=(nballely*1)-(0.5*1)
end do
counter=0
do i=0,nballely-2
  counter=counter+1
  xcd(counter)=(0.5*1)
  ycd(counter)=(nballely*1)-(0.5*1)-(i*1)
end do

!!!----- Outer convex hull (Coordinates) ----!!!
counter=0
do j=invt+1,invr
  counter=counter+1
  xcoord(counter)=kca(1)+(r*cos(rad*j))
  ycoord(counter)=yca(1)+(r*sin(rad*j))
end do
do i=2,nballelx-1
  do j=invt+1,invr
    counter=counter+1
    xcoord(counter)=kca(i)+(r*cos(rad*j))
    ycoord(counter)=yca(i)+(r*sin(rad*j))
  end do
end do
do j=invt+1,inkr
  counter=counter+1
  xcoord(counter)=kcb(1)+(r*cos(rad*j))
  ycoord(counter)=ycb(1)+(r*sin(rad*j))
end do
do i=2,nballely-1
  do j=invt+1,inkr
    counter=counter+1
    xcoord(counter)=xcb(i)+(r*cos(rad*j))
    ycoord(counter)=ycb(i)+(r*sin(rad*j))
  end do
end do

```

:bottom grains!

:right hand grains!

:Top grains!

:left hand grains!

:first grain of bottom sequence (bottom left)!

:additional grains (bottom, left to right)!

:first grain of right hand sequence (bottom right)!

:additional grains (right hand, going up)!

Part 3a: computing the coordinates of the vertices on all surfaces

```

do j=1:nv+1,invr
  counter=counter+1
  xcoord(counter)=xcc(1)+(r*cos(rad*j))
  ycoord(counter)=ycc(1)+(r*sin(rad*j))
end do
do i=2:nballsx-1
  do j=1:nv+1,invr
    counter=counter+1
    xcoord(counter)=xcc(1)+(r*cos(rad*j))
    ycoord(counter)=ycc(1)+(r*sin(rad*j))
  end do
end do
do j=1:nv+1,invr
  counter=counter+1
  xcoord(counter)=xcd(1)+(r*cos(rad*j))
  ycoord(counter)=ycd(1)+(r*sin(rad*j))
end do
do i=2:nballsy-1
  do j=1:nv+1,invr
    counter=counter+1
    xcoord(counter)=xcd(1)+(r*cos(rad*j))
    ycoord(counter)=ycd(1)+(r*sin(rad*j))
  end do
end do
!!!----- Inner convex hull -----!!!
counter=0
do i=1,total
  do j=1:nv+1,invr
    counter=counter+1
    xpores(counter)=spx(1)-(0.5*(1)+(r*cos(rad*j)))
    ypores(counter)=spy(1)-(0.5*(1)+(r*sin(rad*j)))
  end do
  do j=1:nv+1,invr
    counter=counter+1
    xpores(counter)=spx(1)-(0.5*(1)+(r*cos(rad*j)))
    ypores(counter)=spy(1)+(0.5*(1)+(r*sin(rad*j)))
  end do
  do j=1:nv+1,invr
    counter=counter+1
    xpores(counter)=spx(1)+(0.5*(1)+(r*cos(rad*j)))
    ypores(counter)=spy(1)-(0.5*(1)+(r*sin(rad*j)))
  end do
  do j=1:nv+1,invr
    counter=counter+1
    xpores(counter)=spx(1)+(0.5*(1)+(r*cos(rad*j)))
    ypores(counter)=spy(1)+(0.5*(1)+(r*sin(rad*j)))
  end do
end do

```

!first grain top sequence (top right)!

!additional grains (top sequence, right to left)!

!first grain left sequence (top left)!

!additional grains (left sequence, going down)!

!first (bottom left) sequence!

!second (top left) sequence!

!third (top right) sequence!

!fourth (bottom right) sequence!

Part 3b: computing the coordinates of the vertices on all surfaces (continued 1)


```

!!!----- Additional points Resolution -----!!!

counter=0
do i=1,nballsx
  do j=1,nballsy-1
    counter=counter+1
    tx(counter)=i*h
    ty(counter)=j*h
  end do
end do

counter=0
do j=1,vsPRES
  do i=0,ihTA-1
    counter=counter+1
    resx(counter)=tx(j) - (0.5*h) - h*(sp)+(1*sp)
    resy(counter)=ty(j)
  end do
end do

counter=0
do i=1,nballsx
  do j=1,nballsy-1
    counter=counter+1
    vty(counter)=i*h
    vtx(counter)=j*h
  end do
end do

counter=0
do j=1,vsPRES
  do i=0,ihTA-1
    counter=counter+1
    vresy(counter)=vty(j) - (0.5*h) - h*(sp)+(1*sp)
    vresx(counter)=vtx(j)
  end do
end do

!!!----- Additional points Resolution -----!!!

;computing locations of additional points (horizontal direction);

counter=0
do i=1,nballsx
  do j=1,nballsy-1
    counter=counter+1
    tx(counter)=i*h
    ty(counter)=j*h
  end do
end do

;computing locations of additional points (vertical direction);

counter=0
do i=1,vsPRES
  do j=0,ihTA-1
    counter=counter+1
    resx(counter)=tx(j) - (0.5*h) - h*(sp)+(1*sp)
    resy(counter)=ty(j)
  end do
end do

;computing exact coordinates of vertical additional points;

counter=0
do j=1,vsPRES
  do i=0,ihTA-1
    counter=counter+1
    vresy(counter)=vty(j) - (0.5*h) - h*(sp)+(1*sp)
    vresx(counter)=vtx(j)
  end do
end do

```

Part 3c: computing the coordinates of the vertices on all surfaces (continued 2)

```

!!!----- Writing File (Part 4) -----!!!
open(unit=345,file='optres.poly', action='write')
write(345,*) pnp+pores+arh+arv,2,0,0
open(unit=345,file='optres.poly', action='write')
do ip=1,pnp
  write(345,*) number(ip),xcoord(ip),ycoord(ip)
end do
! open(unit=345,file='optres.poly', action='write')
do ip=1,pores
  write(345,*) number(ip+pnp),xpores(ip),ypores(ip)
end do

open(unit=345,file='optres.poly', action='write')
do ip=1,arh
  write(345,*) number(ip+pnp+pores),resx(ip),resy(ip)
end do
open(unit=345,file='optres.poly', action='write')
do ip=1,arv
  write(345,*) number(ip+pnp+pores+arh),vresx(ip),vresy(ip)
end do

open(unit=345,file='optres.poly', action='write')
write(345,*) pnp+pores,1
do ip=1,pnp
  write(345,*) number(ip),number(ip), segment(ip)
end do
open(unit=345,file='optres.poly', action='write')
do ip=1,pores
  write(345,*) number(ip+pnp),number(ip+pnp),segpores(ip)
end do

open(unit=345,file='optres.poly', action='write')
write(345,*) spaces
do ip=1,spaces
  write(345,*) ip, spacex(ip), spacey(ip)
end do
close(345)

```

!total number of points, dimension, #attributes, #boundary markers!

!writing coordinates outer convex hull!

!writing coordinates inner convex hull!

!writing coordinates additional points (X-direction)!

!writing coordinates additional points (Y-direction)!

!total segments!

!writing segments outer convex hull!

!writing segments inner convex hull!

!writing locations of spaces!

```

deallocate(number)
deallocate(segment)
deallocate(segpores)
deallocate(xca)
deallocate(yca)
deallocate(xcb)
deallocate(ycb)
deallocate(xcc)
deallocate(ycc)
deallocate(xcd)
deallocate(ycd)
deallocate(xcoord)
deallocate(ycoord)
deallocate(xpores)
deallocate(ypores)
deallocate(spacex)
deallocate(spacey)
deallocate(spx)
deallocate(spy)
deallocate(ty)
deallocate(tx)
deallocate(vty)
deallocate(vtx)
deallocate(fresx)
deallocate(fresy)
deallocate(vresx)
deallocate(vresy)

call system ('triangle -p optres.1')
call system ('showme optres.2')

!triangle calls .poly file "optres.1"
!triangles refines mesh of optres.1.poly, angle constraint, delaunay!
!showme provides a visual of generated files!

!open(unit=7, file='optres.2.nod')
!read(7,*) np
!close(7)
!open(unit=8, file='optres.2.ela')
!read(8,*) nel
!close(8)

!call output_for_paraview (np,nel,x,y,icon)

end program

```